Chinese Chemical Letters 37 (2026) 112555

Contents lists available at ScienceDirect

Chinese Chemical Letters

journal homepage: www.elsevier.com/locate/cclet

Recent progress in catalysts for direct catalytic decomposition of N_2O

Yingxue Lu[a], Ying Xin[a,b,*], Hao Wu[a], Jin Wang[a,b], Zhaoliang Zhang[a,b,*]

[a] School of Chemistry and Chemical Engineering, University of Jinan, Ji'nan 250022, China
[b] Shandong Key Laboratory of Green and Low Carbon Recycling and Application of Rare Earth Materials, Jining 272600, China

ARTICLE INFO

Article history:
Received 30 October 2025
Revised 16 January 2026
Accepted 26 February 2026
Available online 27 February 2026

Keywords:
N_2O decomposition
Catalyst
Reaction mechanism
Noble metal
Transition metal oxide
Zeolite

ABSTRACT

Nitrous oxide (N_2O), a potent greenhouse gas, requires urgent and effective mitigation strategies. Among traditional (high-temperature thermal decomposition, selective catalytic reduction (SCR), direct catalytic decomposition, *etc.*) and emerging (biological treatment, photo/electrocatalysis, plasma-assisted decomposition, *etc.*) technologies, direct catalytic decomposition stands out as a highly promising approach thanks to its energy efficiency and environmental benefits. This review systematically summarizes recent progress in the catalytic decomposition of N_2O, with emphasis on catalysts, including noble metal catalysts, transition metal oxide catalysts, zeolite-based catalysts, and emerging catalytic materials. Atomic-level active site engineering, oxygen vacancy modulation, and active site-support interactions, which determine catalytic performances and reaction mechanisms, are critically delineated. Furthermore, practical challenges of catalyst designs and integrated reaction systems are addressed. By establishing connections between fundamental research and industrial applications, this review proposes a comprehensive framework for the development of next-generation N_2O decomposition catalysts, thereby supporting global efforts to cut greenhouse gas emissions.

© 2026 Published by Elsevier B.V. on behalf of Chinese Chemical Society and Institute of Materia Medica, Chinese Academy of Medical Sciences.

1. Introduction

In the context of escalating global climate change, nitrous oxide (N_2O) has drawn increasing concern as a potent greenhouse gas with profound impacts on the environment, ecology, and public health (Fig. 1) [1]. Despite its low atmospheric concentration, N_2O possesses a global warming potential (GWP) that is approximately 310 times that of carbon dioxide (CO_2) and 21 times that of methane (CH_4) over a 100-year time scale [2]. Notably, emissions from agricultural activities, industrial sources, and vehicles are notably persistent, with an estimated atmospheric lifespan of about 116 ± 9 years, exacerbating stratospheric ozone depletion and posing growing risks to human and environmental health (Fig. 1) [3–6]. As the global population continues to expand and economies advance, the intensity of the emission sources increases, leading to a continuous rise in atmospheric N_2O levels [7]. Specifically, the Euro VII emission regulations have formally introduced a control standard for the emission of this greenhouse gas [8]. In August 2025, China issued the "Action Plan for Nitrous Oxide Emission Control in the Industrial Sector" [9]. Consequently, it is imperative to implement effective measures to mitigate N_2O emissions.

A range of technologies for reducing N_2O emissions have been investigated, including thermal decomposition, selective catalytic reduction (SCR), direct catalytic decomposition, and other emerging approaches [10–15]. Among them, high-temperature thermal decomposition, which cleaves the N—O bond to form N_2 and O_2, typically requires high temperatures between 800 °C and 1000 °C, resulting in significant energy consumption and stringent equipment requirements, thereby limiting its scalability [16]. Selective catalytic reduction (SCR) technology employs a reducing agent (*e.g.*, NH_3, urea, H_2, CO, hydrocarbons) and a catalyst to selectively convert N_2O to N_2 [17,18]. Although its industrial adoption, SCR introduces secondary pollution and increases economic costs associated with reductant handling and consumption. Conversely, direct catalytic decomposition reduces the activation energy required for N—O bond cleavage by using catalysts, thereby enabling efficient conversion at moderate temperatures (250–500 °C) without the necessity for external reductants [10]. This approach entails a substantial reduction in energy input, facilitates streamlined process design, circumvents high-temperature corrosion and safety concerns, and eliminates secondary pollutants. The aforementioned advantages render it particularly suitable for the treatment of high-concentration N_2O, exhibiting high conversion efficiency. In addition to above conventional methods, several alternative strategies have been explored, including adsorption separation, biological treatment, photo/electrocatalysis, and plasma-assisted decom-

* Corresponding authors.
E-mail addresses: chm_xiny@ujn.edu.cn (Y. Xin), chm_zhangzl@ujn.edu.cn (Z. Zhang).

https://doi.org/10.1016/j.cclet.2026.112555
1001-8417/© 2026 Published by Elsevier B.V. on behalf of Chinese Chemical Society and Institute of Materia Medica, Chinese Academy of Medical Sciences.

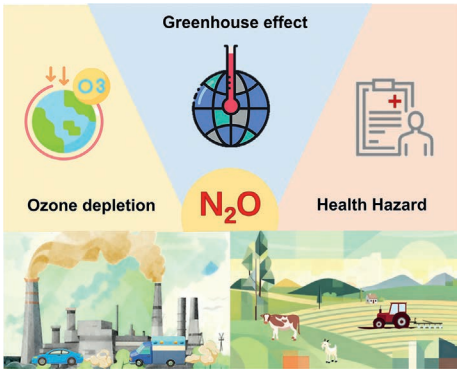


Fig. 1. N_2O emission sources and hazards.

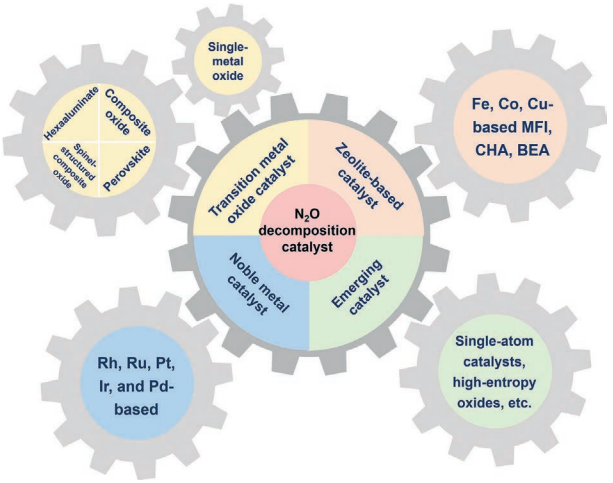


Fig. 2. Catalysts for the direct catalytic decomposition of N_2O.

position [19–23]. As the emerging technologies, their practical application is currently hindered by high energy requirements, low efficiency and unfavorable economics.

Direct catalytic decomposition has become the predominant and extensively utilized technology for N_2O abatement owing to its efficiency, cost-effectiveness, and environmental friendliness [16], where catalysts play a decisive role in determining both activity and durability in this process. As such, the present review focuses on several categories of catalyst, including noble metal catalysts, transition metal oxides, zeolite-based materials, and other novel systems (Fig. 2), providing recent experimental and theoretical research progress [24,25]. The integration of fundamental understanding with practical performance is intended to delineate a roadmap for the rational design of next-generation N_2O decomposition catalysts and proposing innovative solutions for the future research.

2. Catalysts for N_2O decomposition

2.1. Noble metal catalysts

Noble metal catalysts are the first catalysts utilized for N_2O decomposition and have been extensively studied due to their exceptional catalytic efficiency at low temperatures [26,27]. Despite their high activity, these catalysts face scarcity, non-renewability, high cost, susceptibility to deactivation, and limited practical applications. Among Rh, Ru, Pt, Ir, and Pd supported on Al_2O_3, CeO_2, SiO_2, and ZrO_2, the order of catalytic activity is typically as follows: Rh > Ru ≈ Ir ≈ Ag > Pt > Pd, with Rh-, Ru-, and Ir-based catalysts being the most extensively studied ones [28]. This section provides a comprehensive overview of noble metal catalysts employed in N_2O decomposition, detailing preparation methods, noble metal precursor types, support composition and structure, and the effect of promoter incorporation on catalytic performance.

The catalytic performance of noble metal catalysts in N_2O decomposition is significantly affected by their preparation methods, which dictate metal dispersion, particle size, and surface chemistry. Common techniques employed in this field include impregnation (IMP), hydrothermal synthesis (HS), co-precipitation (COP), deposition-precipitation (DP) and ethylene glycol reduction (EGR). For instance, Ru/Al_2O_3 synthesized *via* EGR achieved high dispersion and small nanoparticles (≤3 nm), resulting in superior activity, while the DP method enhanced metal-support interactions and thus creating electron-deficient sites [29]. In contrast, IMP can lead to prevalent metallic sites or poisoning by residual species (*e.g.*, Cl^-), although pre-treatment or cyclic operation can alleviate these effects [30]. Electrodeposition produces Rh/Mg/Al catalysts on Fe-CrAlloy foams with uniform coatings, reduced activation energy, and 51 % conversion retention after 24 h at 475 °C with 2.0 ± 1.1 nm Rh nanoparticles [31]. The selection of metal precursors also exerts a substantial influence on the density and accessibility of active sites, thereby affecting the catalytic performance. Chloride-based precursors (*e.g.*, $RhCl_3$) frequently result in site blocking, whereas nitrate-derived catalysts circumvent such complications [32]. Moreover, post-synthetic treatments, such as calcination atmosphere, further influence catalytic behavior [33].

Support materials govern reactivity *via* electronic effects, oxygen mobility, and interfacial synergy [26,34]. Mesoporous supports enhance metal dispersion and accessibility [35,36], and redox-active supports, such as ZrO_2 and CeO_2, facilitate the formation and replenishment of oxygen vacancy (O_v), which is crucial for the rate-determining O_2 desorption step [37]. Furthermore, high-temperature steam treatment of the Rh/CeO_2 catalyst activates the lattice oxygen at Rh–CeO_2 interface, which facilitates oxygen desorption and enhances the redox cycling stability, thereby lowering the T_{50} by 127 °C relative to the untreated catalyst [38]. Supports with high oxygen lability, such as CeO_2-modified Al_2O_3 (ACZ), improve sintering resistance and stability for Ir nanoparticles (Fig. 3a) [39,40]. Metal phosphates optimize the balance between O_2 binding and desorption, improving both activity and durability [41]. Defect-rich supports increase metal exposure and stability, whereas inert supports often lead to sintering. Furthermore, the defect-rich $La_{1.6}Sr_{0.4}NiO_4$ has been demonstrated to promote oxygen vacancy formation and stabilize active Ru states [42]. Ir supported on Fe-substituted La-hexaaluminate demonstrates exceptional activity (T_{50} = 284 °C) due to the promotion of electron-rich Ir species by O_v, which enhances N_2O activation synergistically [43]. Similarly, defect-rich CeO_2-supported Rh nanoclusters have been observed to exhibit nearly complete metal exposure and optimal intermediate transformation, delivering a turnover frequency 4.6 times higher than that of Rh nanoparticles (Fig. 3b) [44]. The structure, composition, and redox properties of the support are essential in designing active and durable catalysts for N_2O decomposition.

The utilization of promoters has been demonstrated to markedly augment the performance of noble metal catalysts in N_2O decomposition, with enhancements observed in both redox properties and metal-support interactions. For instance, the addition of Ag or Pd to Rh-based catalysts increases reducibility and accelerates O_2 desorption, which is the rate-determining step [45,46]. Furthermore, the modification of Ir has been demonstrated to facilitate oxygen removal (Figs. 3c and d) [47]. The dispersion of alkali metals, such as K, has been observed to enhance surface alkalinity and electron donation, as evidenced in Pt-M/SiO_2 (M = K, Na, Cs) systems, where K enhances both oxygen mobility and catalytic

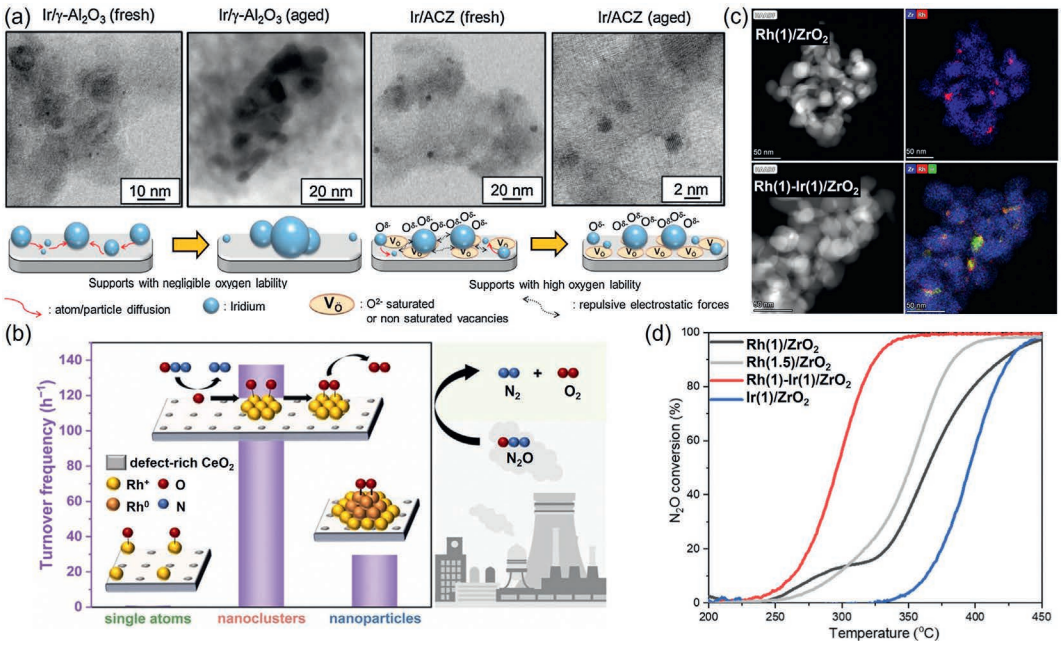


Fig. 3. (a) TEM images and models of fresh and aged Ir/γ-Al_2O_3 and Ir/ACZ. Reproduced with permission [40]. Copyright 2016, Elsevier. (b) Normalized turnover frequency at 250 °C for defect-rich CeO_2 with different morphologies. Reproduced with permission [44]. Copyright 2025, Elsevier. (c) HAADF–STEM and EDX mapping images, and (d) the catalytic activity of Rh(1)/ZrO_2 and Rh(1)–Ir(1)/ZrO_2 for N_2O decomposition. Reproduced with permission [47]. Copyright 2025, American Chemical Society.

activity [48]. However, the presence of inhibitors such as O_2, and H_2O can lead to reversible deactivation.

2.2. Transition metal oxide catalysts

Transition metal oxides are the focus of significant research due to their advantageous redox capacity, thermal stability, and cost-effectiveness in the catalytic decomposition of N_2O [49], which can generally be classified into the following categories: single-metal oxides, composite oxides, hexaaluminates, spinel-structured composite oxides, and perovskite oxides. Each of these exhibits unique benefits and catalytic mechanisms.

2.2.1. Single-metal oxides

Single metal oxides are composed of straightforward compositions and easy to prepare. Amongst, Co_3O_4 exhibited remarkable catalytic efficiency, thus promoting deep investigation [50]. In the study by Ma *et al.*, the synthesis of ordered mesoporous single-metal oxides was conducted, which exhibited superior catalytic activity in N_2O decomposition when compared to commercial counterparts [51]. Stelmachowski *et al.* produced Co_3O_4 with diverse morphologies, finding that the catalyst calcined at 600 °C exhibited optimal activity due to its crystalline structure [52]. The findings of the study demonstrated that larger, more crystalline particles exhibited superior catalytic performance in comparison to their smaller counterparts. The unique properties of nanocubic Co_3O_4 were identified as the primary factor contributing to its enhanced catalytic performance (Figs. 4a and b) [53]. Yu *et al.* developed a Co_3O_4 catalyst with a "Yardang Landform" microstructure, which demonstrated high activity and stability under industrial conditions for N_2O decomposition [54]. In addition to structural optimization, the refinement of synthesis conditions has been shown to markedly enhance the catalytic performance in N_2O decomposition. The selection of precursor is of crucial importance, with β-$Co(OH)_2$-derived catalysts demonstrating superior performance due to improved Co^{3+} reducibility and defect-rich structures [55]. O_v concentration is also pivotal, with the Mars-van Krevelen mechanism driving the reaction. Li *et al.* determined

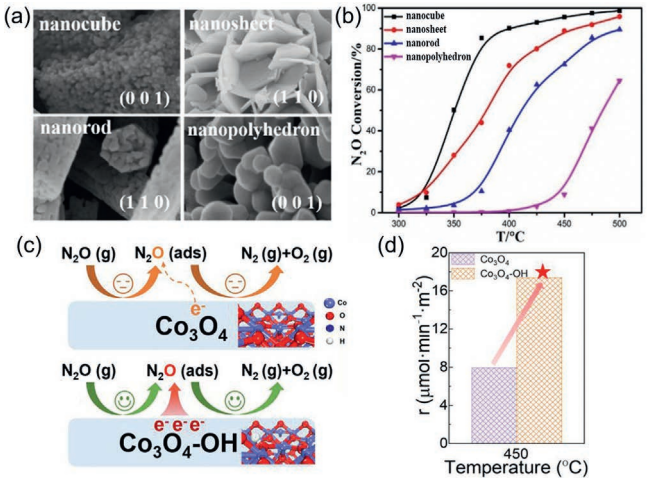


Fig. 4. (a) SEM images and (b) N_2O conversions of Co_3O_4 with different morphologies. Reproduced with permission [53]. Copyright 2021, Elsevier. (c) Hydroxyl group facilitated mechanism for N_2O decomposition activity on the Co_3O_4 surface and (d) normalized reaction rates of Co_3O_4 and Co_3O_4-OH. Reproduced with permission [59]. Copyright 2025, American Chemical Society.

the optimal hydrothermal synthesis conditions for Co_3O_4 catalysts, achieving 91 % N_2O conversion at 400 °C in oxygen/steam atmospheres [56]. This was attributed to specific morphologies, weakened Co^{3+}–O^- bonds, and an enhanced Co^{2+}/Co^{3+} ratio. Polyvinyl alcohol (PVA) modification has been demonstrated to enhance the performance of the Co_3O_4 catalyst, with improvements being observed in both the surface Co^{2+} concentration and the O_v density [57]. This enhancement is further confirmed by DFT calculations, which indicated that Co^{2+} is the preferred site for N_2O adsorption. The employment of formic acid-treated Co_3O_4 catalysts results in enhanced N_2O decomposition activity, attributable to increased surface area, elevated Co^{3+} concentration, augmented reducibility, and enhanced oxygen desorption capacity [58]. Despite the divergent views amongst researchers regarding the role of Co

ions, it is evident that Co^{2+} sites facilitate N_2O adsorption and activation, while Co^{3+} sites promote oxygen desorption. The overall activity of the catalyst is contingent upon a balanced Co^{2+}/Co^{3+} ratio and the specific reaction conditions. Very recently, hydroxyl groups (−OH) were introduced onto Co_3O_4 *via* hydrothermal treatment, significantly enhancing N_2O decomposition activity by facilitating electron transfer at the gas-solid interface (Figs. 4c and d) [59]. Electronic structure analysis and DFT simulations confirmed that −OH groups donate electrons to N_2O, weakening the N–O bond and lowering the activation barrier.

2.2.2. Composite oxides

Comparing with single-metal oxides that exhibit basic and limited catalytic functionality, mixed-metal oxides with precise stoichiometries and well-defined crystal structures often outperform them in N_2O decomposition, which are typically engineered through the introduction of heteroatoms into oxides to modulate the electronic structure and/or induce defects for O_v formation. Based on the underlying regulation mechanisms, these strategies may be classified into three distinct types.

(1) Alkali and alkaline earth metals

Alkali metals (*e.g.*, Li, Na, K, Rb, and Cs) significantly enhance the performance of N_2O decomposition over transition metal oxide catalysts, primarily *via* electronic donation and work function reduction [60,61]. For instance, the introduction of Na into Co_3O_4 significantly enhances the low-temperature activity of N_2O decomposition by facilitating Co^{3+}/Co^{2+} cycling and electron donation [62]. K lowers the T_{50} (temperature for 50% conversion) by 150 °C for both Co_3O_4 and Mn_3O_4 by forming a K^+–O_{surf}^- dipole that reduces the work function and promotes oxygen desorption, with optimal activity at 2–8 atoms/nm^2 [63]. Similarly, the light-off temperature for K-doped $Zn_{0.4}Co_{2.6}O_4$ is reduced to ∼150 °C, attributing to the weakened Co−O bonds derived from the electronic effect of K, which also acts as the sacrificial site for SO_2 adsorption, thus inhibiting the deactivation of the catalyst [64,65]. A monolayer of Cs on Co_3O_4 forms Cs−O−Co sites *via* 6s–2p orbital hybridization, generating abundant Co^{2+} and achieving over 95% N_2O conversion at 300 °C, though bulk doping leads to inactive Cs_2O_2/CsOH phases (Figs. 5a and b) [66,67]. $Cs_{0.1}$-Co_3O_4 exhibits 39.5 times greater activity in comparison with pure Co_3O_4 and resists O_2 inhibition [68]. However, Cs does not enhance the activity of oxides such as CuO or NiO, which indicates the importance of support-alkali metal interactions (Figs. 5c and d) [66]. *In situ* DRIFTS and DFT studies highlight the roles of O_2 desorption kinetics and frontier orbital alignment.

Comparatively, alkaline-earth metals (Mg, Ca, Sr, Ba) enhance catalysts *via* lattice distortion and improved redox properties [69]. In $A_{0.5}Co_{2.5}O_4$ (A = Mg, Ca, Sr, Ba), Ca, Sr, or Ba facilitates the reduction of Co^{3+} to Co^{2+}, increasing O_v concentration and weakening Co−O bonds, with Ba showing the best performance (Figs. 5e and f) [70]. Ca-doped Co_3O_4 with a Ca/Co molar ratio of 1:2 shows remarkable activity, reaching 100% N_2O conversion at 400 °C [71]. This is due to preferential exposure of the (111) crystal plane and abundant surface oxygen. Core-shell structured $Co_{0.24}Ba$ catalysts (Co_3O_4 on $BaCO_3$) use only 8.91 wt% Co_3O_4 to achieve complete N_2O decomposition at 400 °C [72]. Alkaline-earth metals (Mg < Ca < Sr < Ba) are generally weaker promoters than alkali metals (Li < Na < K < Rb < Cs), with the effect of primarily modulating lattice oxygen mobility rather than electronic promotion [73]. DFT calculations confirm that larger dopants (*e.g.*, Ba, Sr) induce greater lattice distortion, thereby improving N_2O adsorption and O_2 desorption.

In addition to alkali and alkaline earth metals, other main-group metal elements (*e.g.*, Bi, Sn) dopants have been demonstrated to enhance the catalytic performance of N_2O decomposition through electronic and structural modifications. The Bi-enhanced Co_3O_4 maintains a unique "Yardang Landform" microstructure, which exposes high-activity crystal planes (*e.g.*, (422), (533), and (620)) that weaken the Co−O bonds [74]. The 3.0F-$Bi_{0.015}Co$ catalyst achieves > 88% N_2O conversion at 300 °C and is resistant to O_2, H_2O, and NO [75]. The incorporation of Bi into NiO has been shown to increase both O_v and Ni^{3+} sites, whilst simultaneously forming inactive Bi_2O_3 at high loading. SnO_2-Co_3O_4 composites utilize interfacial interactions in order to boost Co^{2+} electron donation and improve Co_3O_4 dispersion [76].

In summary, the introduction of alkali and alkaline-earth metals primarily serves as an electronic promoter, which facilitates the key O_2 desorption step by lowering the work function and optimizing the surface electron density. Beyond simple electronic donation, the incorporation of redox-active elements, such as rare-earth and transition metal elements, offers a more dynamic pathway to enhance the catalytic cycle.

(2) Rare-earth and transition metals

The doping of rare-earth elements (Ce, Sm, Gd, Eu) into metal oxides has been demonstrated to enhance the catalytic performance of N_2O decomposition, which is achieved by modulating the concentration of O_v, the redox kinetics, and the electronic interactions. In the Co_3O_4-CeO_2 systems, the incorporation of Ce promotes the O_v formation, thereby enabling $Co^{2+} + Ce^{4+} \leftrightarrow Co^{3+} + Ce^{3+}$ redox cycles [77]. The Co_2Ce_1 oxide exhibits a N_2O conversion of over 95% at 300 °C (Figs. 6a and b). CeO_2 nanorods with {100/{110} facets optimize Co exposure and outperform nanocubes/polyhedral [78,79]. Furthermore, CuO–CeO_2 nanorods exhibit lower activation energy of 87 kJ/mol, due to efficient Cu^{2+}/Cu^+ and Ce^{4+}/Ce^{3+} cycling [80,81]. Sm-doped Co_3O_4 induces distortion and enables $Co^{3+} + Sm^{2+} \leftrightarrow Co^{2+} + Sm^{3+}$ (Figs. 6c and d), while Gd doping increase in the Co^{3+}/Co^{2+} ratio, and weakens Co−O bonds [82,83]. In the case of Pr-doped NiO, the superior catalytic activity (T_{100} = 400–440 °C) and notable resistance to impurity gases (O_2 and NO) in simulated nitric acid exhaust are achieved by the promoted Ni^{2+}/Ni^{3+} redox cycle and regeneration of active Ni^{2+} sites [84]. $Eu_{0.04}Ni$ shifts the reaction mechanism from Langmuir–Hinshelwood (L−H) to Eley–Rideal (E−R), lowering the O_2 desorption barrier and achieving 100% conversion at 400 °C with high impurity tolerance [85]. Furthermore, rare-earth elements also improve bimetallic systems: Nd-doped $Cu_{0.8}Al_{0.2}$ and $Co_{0.8}Al_{0.2}$ oxides form active $CuNd_2O_4$/$NdCoO_3$ phases, lowering the full N_2O conversion temperature by 100 °C [86,87]. In the Ce/Ba−NiO system, Ce inhibits NiO crystallization while Ba weakens Ni−O bonds, enabling complete N_2O decomposition at 300 °C even with 5% O_2 [88]. Dual promoters (*e.g.*, Dy/K-Co_3O_4, Ba/Ce-CuO) further enhance impurity tolerance (Fig. 6e) [89,90].

Transition metal doping demonstrates notable efficacy in N_2O decomposition through O_v generation, redox promotion, and metal-support interactions. Bimetallic Cu_xCo_y and Cu_xMn oxides exhibit enhanced performance in comparison to single-metal oxides: Co_3O_4 offers abundant O_v sites for N_2O adsorption (forming □−Co−ON_2), while CuO or Mn_2O_3 enhances reducibility for N−O cleavage and O_v regeneration [91,92]. Very recently, Long *et al.* partially substituted Mn into octahedral Co^{3+} sites of Co_3O_4 to generate heterointerfaces between δ-MnO_2 and $Co_{3-x}Mn_xO_4$ [93]. The enhanced hybridization between Co 3d and O 2p orbitals and high Co−O−Mn covalency lead to the formation of highly active lattice oxygen species, thereby enhancing N_2O decomposition activities and stability. Supports such as *m*-ZrO_2 strengthen metal-support interactions, increasing Co^{2+} and O_v density in Co_3O_4/*m*-ZrO_2, while $Co_3O_4/CaCO_3$ attains complete N_2O conversion at 300 °C with highly dispersed Co_3O_4 [94,95]. Moreover, the morphology of the support plays a pivotal role: CeO_2 nanorods in CuO/CeO_2 favor {100}/{110} exposure, whereas Ni/CeO_2 nanocubes exhibit superior

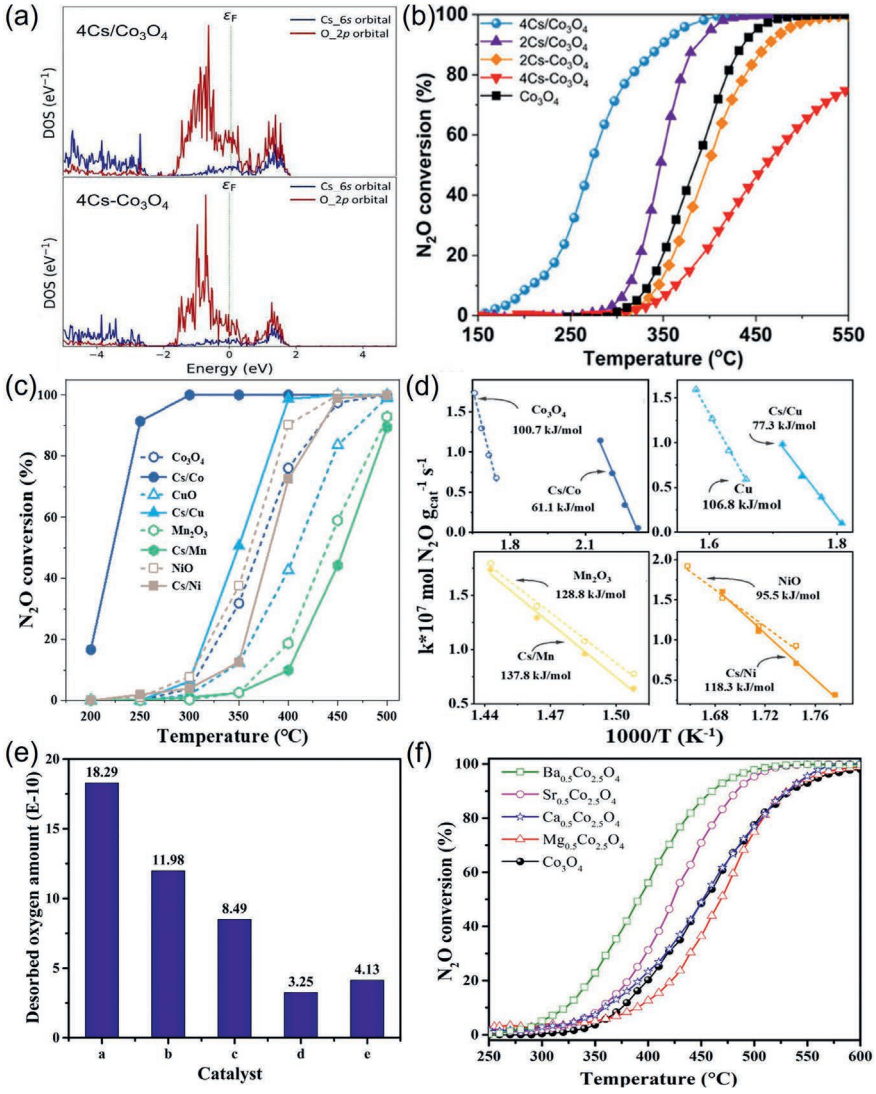


Fig. 5. (a) The density of states functions of the Cs−O−Co band and (b) catalytic performance of N_2O decomposition for 4Cs/Co_3O_4 and 4Cs-Co_3O_4. Reproduced with permission [67]. Copyright 2023, American Chemical Society. (c) N_2O catalytic decomposition performance and (d) Arrhenius plots of N_2O conversion over Cs supporting on different metal oxides. Reproduced with permission [66]. Copyright 2022, American Chemical Society. (e) Integral area of O_2-TPD profiles and (f) N_2O decomposition activity of $Ba_{0.5}Co_{2.5}O_4$, $Sr_{0.5}Co_{2.5}O_4$, $Ca_{0.5}Co_{2.5}O_4$, $Mg_{0.5}Co_{2.5}O_4$, and Co_3O_4. Reproduced with permission [70]. Copyright 2021, American Chemical Society.

activity due to the presence of more NiO clusters and Ni−O−Ce sites [80,96]. The egg-shell-type Cu/γ-Al_2O_3 catalyst with a reducible Cu^+ shell demonstrates superior stability under temperature, air, and steam conditions [97]. Substitutional doping (*e.g.*, Cd^{2+} in NiO, and Co^{3+} in MnO_2) also optimizes O_v formation and redox behavior, and synergistic systems, such as Co_xTi oxides, maintain 100% conversion for 30 h, even in the presence of O_2, H_2O, and NO [98–100]. Additionally, Zn doping in Co_3O_4/CeO_2 catalyst ($Co_{2.4}Zn_{0.6}O_4/CeO_2$) significantly improved the overall N_2O decomposition performance, evidenced by a 110 °C decrease in T_{90} and robust tolerance to O_2, NO_x, and H_2O [101].

The strategies previously discussed highlight the critical role of rare-earth and transition metal dopants, which modify the host oxide by tuning the redox properties and O_v dynamics. In addition to the metallic elements, the introduction of non-metallic elements has the potential to enhance the catalytic performance.

(3) Non-metal dopants

Non-metallic (*e.g.*, N, F) dopants improve the catalytic performance of N_2O decomposition, primarily by introducing defects and facilitating electronic redistribution. N-doped Co_3O_4 (N-Co_3O_4−0.05) achieves 100% N_2O conversion at 380 °C, which is 160 °C lower than that of pristine Co_3O_4 [102]. This phenomenon can be attributed to N-induced O_v, higher Co^{2+} density, and increased basicity. F-doped Co_3O_4, where F substitutes for lattice oxygen, increases surface area and basicity, thereby lowering the temperature for complete N_2O conversion to 380 °C, while maintaining stability in O_2 and H_2O [103]. Non-metal doping offers a viable route to induce defects and modify surface electronic properties, thereby boosting N_2O decomposition performance.

The above-discussed doping or strategic addition of metals and nonmetals has been demonstrated to modulate the surface properties of these catalysts by improving electron transfer, generating O_v, weakening metal−O bonds, and accelerating redox/O_2 desorption kinetics. It has been demonstrated that these alterations increase intrinsic activity and resistance to O_2, H_2O, and NO, and thus providing a framework for developing high-performance N_2O decomposition catalysts. The integration of defect engineering, electronic tuning, and morphological control highlights the potential of mixed-metal oxides in industrial catalysis.

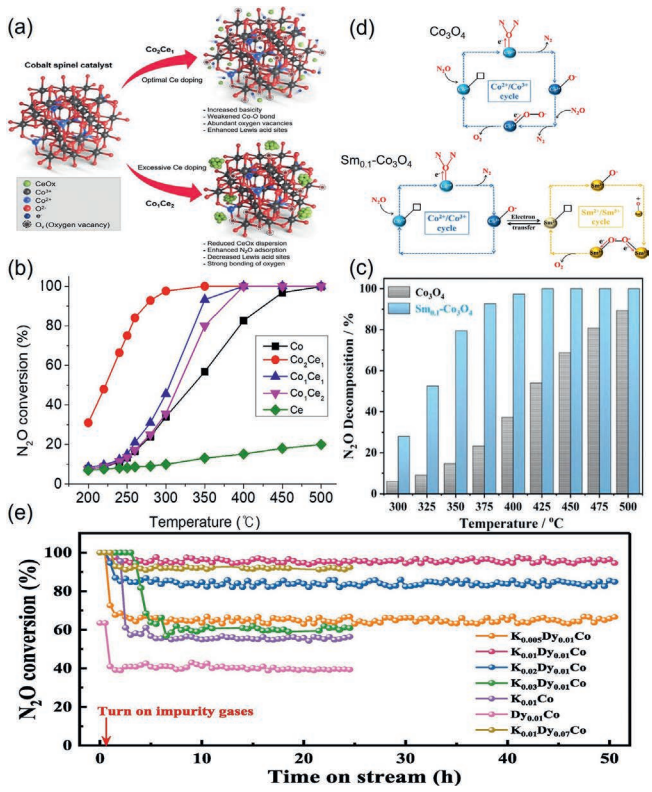


Fig. 6. (a) Reaction pathways and (b) catalytic performance for N_2O decomposition over Co_xCe_y binary oxide catalysts. Reproduced with permission [77]. Copyright 2025, Elsevier. (c) N_2O decomposition performance as a function of the reaction temperature and (d) electron transfer pathway in N_2O decomposition for Co_3O_4 and $Sm_{0.1}$-Co_3O_4. Reproduced with permission [82]. Copyright 2021, Elsevier. (e) N_2O conversion over $Dy_{0.01}Co$, $K_{0.01}Co$, $K_yDy_{0.01}Co$ ($y = 0.005$, 0.01, 0.02, 0.03) and $K_{0.01}Dy_{0.07}Co$ catalysts at 400 °C changed with time on stream. Reproduced with permission [89]. Copyright 2025, Elsevier.

2.2.3. Hexaaluminates

Beyond supported or doped oxide systems, well-defined crystalline structures such as hexaaluminates ($ABAl_{11}O_{19}$, where A = La, Ba and B = Mn, Fe, Ni) offer distinct advantages for high-temperature N_2O decomposition featuring enhanced thermal/chemical stability and cost-effectiveness [104]. Fe- and Mn-substituted hexaaluminates exhibit high activity that are largely independent of the A-site cations (La or Ba), while the activity of Ni-substituted hexaaluminates adheres to a similar perform as unsubstituted counterparts [105]. The catalytic performance of the hexaaluminates is principally determined by the occupancy of specific sites within their crystal structure. In $LaFe_xAl_{12-x}O_{19}$, Fe^{3+} ions demonstrate a clear preference for occupying tetrahedral Al(2) and trigonal bipyramidal Al(5) sites within the magnetoplumbite structure, with octahedral Al(3) sites in the mirror plane exhibiting particular activity with regard to N_2O decomposition [106]. It is noteworthy that Fe^{3+} ions derived from perovskite-type $LaFeO_3$ intermediates show a marked preference for occupying these octahedral Al(3) sites, while the presence of Fe^{2+} species has a detrimental effect on activity. In the context of $BaFe_xAl_{12-x}O_{19}$, the stabilization of Fe^{3+} follows a dual-phase mechanism. In the context of low Fe contents ($x = 1$–4), Fe^{3+} occupies tetrahedral Al(5) sites within the β_1-Al_2O_3 phase. In contrast, at higher loadings ($x = 5$–12), excess Fe^{3+} is accommodated in trigonal bipyramidal Al(5) and octahedral Al(3) sites within the magnetoplumbite phase [107]. The latter is particularly crucial for N_2O activation. La-hexaaluminates surpass Ba-based ones by substituting a great number of Al sites in the exposed mirror plane, thus enhancing access to active Fe^{3+} centers.

2.2.4. Spinel-structured composite oxides

Spinel-structured composite oxides (AB_2O_4) have been identified as highly effective N_2O decomposition catalysts, prized for their adjustable redox properties, thermal stability, and O_v generation [108]. Co_3O_4-based spinels have been shown to be particularly active due to the facile reduction of octahedral Co^{3+} to Co^{2+}, which has been demonstrated to promote O_v formation and accelerate O_2 desorption. The Co^{2+}/Co^{3+} ratio exerts a substantial influence on catalytic performance, which can be enhanced through elemental substitution and doping. In the context of $Ni_xCo_{1-x}Co_2O_4$ spinels, partial substitution of Co^{2+} with Ni^{2+} has been demonstrated to enhance activity by reducing crystallite size, increasing surface area, and facilitating Co^{3+} reduction, with optimal performance observed at intermediate Ni loadings [109]. Similarly, $Zn_xCo_{1-x}Co_2O_4$ has been demonstrated to exhibit superior activity in N_2O decomposition at low temperatures, with $ZnCo_2O_4$ achieving 50% N_2O conversion at 177 °C (Fig. 7a) [110]. Furthermore, Mn- and Zn-substituted ferrites ($Mn_xFe_{1-x}Fe_2O_4$, $Zn_xFe_{1-x}Fe_2O_4$) have also been observed to demonstrate high activity, with $Mn_{0.8}Fe_{0.2}Fe_2O_4$ and $Zn_{0.6}Fe_{0.4}Fe_2O_4$ reaching complete N_2O conversion at 250 °C and 280 °C, respectively, although they are susceptible to O_2 inhibition [111].

2.2.5. Perovskite oxides

Perovskite-type oxides (ABO_3), with A-site cations as rare-earth or alkaline-earth metals and B-sites as transition metals, exhibit exceptional catalytic performance in N_2O decomposition [112]. For instance, $LaCoO_3$ exhibits superior activity due to its optimal B-site reducibility linking to O 2p-B 3d covalency and e_g orbital occupancy, which are crucial for N_2O activation and O_2 desorption (Figs. 7b and c) [113]. The synthesis methods significantly impact catalytic properties. The mechanochemical preparation of $LaMnO_3$ under Ar creates oxygen-deficient surfaces, which exhibit enhanced activity in comparison to conventional sol-gel methods [114]. This phenomenon can be attributed to an increased N_2O interaction at O_v. $PrBaCoO_3$, synthesized *via* supercritical antisolvent techniques, has been observed to exhibit high mobile oxygen content and a considerable surface area, resulting in reduced operating temperatures [115]. Alternative methods, such as the thermal decomposition of oxalate/carbonate precursors for $LaNiO_3$, have been demonstrated to preserve high activity while avoiding phase impurities [116]. The B-site identity has been identified as a critical factor in determining performance: ranked as $LaMnO_3$ > $LaCoO_3$ > $LaNiO_3$ > $LaFeO_3$. DFT calculations have attributed $LaMnO_3$'s superior activity to its distinct electronic structure and surface characteristics [117].

Tuning the A-site in ABO_3 perovskites has been shown to significantly boost N_2O decomposition activity by modifying the redox properties of B-sites through charge compensation. In $La_{1-x}Sr_xFeO_3$, optimal Sr substitution ($x = 0.25$) maximizes activity by facilitating reverse oxygen uptake from the lattice [118]. $N_2O^-_{(ads)}$ dissociation has been identified as the rate-determining step in this system. In the case of the Ce/Sr-substituted $LaCo_{0.8}Fe_{0.2}O_3$, La-deficiency and Sr-substitution enhance thermal stability and resistance to deactivation [119]. Sr incorporation stabilizes Co^{3+} and generates O_v, while Ce substitution promotes Co exsolution, deactivating the catalyst. In the case of $Pr_{1-x}Ba_xMnO_3$, 20 mol% Ba substitution ($Pr_{0.8}Ba_{0.2}MnO_3$) maximizes activity by elevating Mn^{4+} content without forming impurity phases, with supported configurations proving industrially viable [120]. In Ruddlesden-Popper perovskites ($La_{2-x}(Sr,Ce)_xNiO_4$), dual Sr-Ce co-doping has been demonstrated to optimize performance: $La_{0.7}Ce_{0.3}SrNiO_4$ demonstrates remarkable resistance to O_2/H_2O, maintaining 100% conversion at 600 °C [121]. This stability is attributed to the stabilization of Ni oxidation states and the promotion of enhanced oxygen vacancy formation.

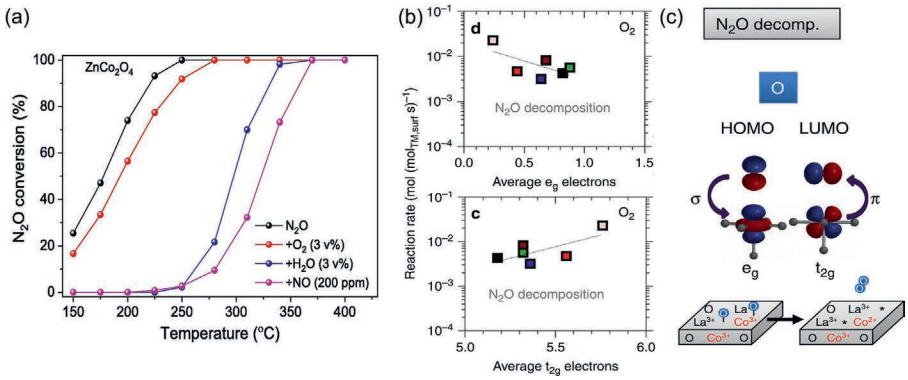


Fig. 7. (a) Catalytic de-N_2O activity of $ZnCo_2O_4$ spinel catalysts. Reproduced with permission [110]. Copyright 2024, Elsevier. (b) N_2O decomposition rates as a function of t_{2g} or e_g orbital occupancy in 0.37 kPa O_2 [Fill colors represent the substituent cation in $LaCoO_3$ (no substituent: black fill): Ni (green), Zn (blue), increasing Al fraction (dark to light red). Lines represent least squares fits of the full set or subset of data] and (c) orbital interactions and the respective kinetically relevant step (KRS) for N_2O decomposition. Reproduced with permission [113]. Copyright 2020, Nature Publishing Group.

B-site doping optimizes catalytic performance for N_2O decomposition through the precise configuration of the active sites and the dynamics of the O_v [122]. In $LaFe_{1-x}Ni_xO_3$ systems, Ni substitution enhances the catalytic activity for N_2O decomposition [123]. In $BaFe_{1-x}Sn_xO_{3-\delta}$, the introduction of Sn results in the formation of 5-coordinated $Fe^{3+}-O_5$ active centers, thus reducing the Fe valence state through the establishment of Fe−O−Sn bonds and the expansion of the unit cell [124]. These modifications leads to a reduction in the activation energy from 241 kJ/mol ($x=0$) to 178 kJ/mol ($x=0.8$), with $BaFe_{0.2}Sn_{0.8}O_{3-\delta}$ exhibiting a 4-fold increase in intrinsic rate compared to undoped $BaFeO_3$. In $CaMn_{0.7}Fe_{0.3}O_{3-\delta}$, the presence of Fe-induced O_v facilitates a regenerative cycle, with activity demonstrating a positive correlation with O_v concentration [125].

A/B-site co-doping and structural modifications also influence the catalytic performance of ABO_3 in N_2O decomposition [126]. $La_{0.75}Sr_{0.25}Co_{0.81}Fe_{0.19}O_x$ has exhibited a T_{50} of 448 °C attributed to weakened Co−O bonds and mobile lattice oxygen species [127]. Support interactions and composite formations critically modulate performance. $LaCoO_3/ZrO_2$-La exhibits enhanced activity due to elevated Co^{2+}/Co^{3+} and $O_{ads.}/O_L$ ratios, with coordinatively unsaturated Co^{2+} acting as the active site [128]. The heterostructured $LaSrFeO_4/La_{0.4}Sr_{0.6}FeO_3$ displays superior performance by combining enhanced surface oxygen exchange rates with preserved bulk oxygen diffusion, attributed to interfacial synergy between the $LaSrFeO_4$ and $La_{0.4}Sr_{0.6}FeO_3$ phases [129].

2.3. Zeolite-based catalysts

Zeolites feature well-defined pore structures, high surface areas, and ion-exchange capabilities, rendering them efficient and economical catalysts for N_2O decomposition [25]. Their catalytic performance is significantly influenced by framework topology, which governs the nuclearity, coordination environment, and spatial distribution of active metal sites (*e.g.*, Fe, Cu, Co) (Figs. 8a and b) [130]. A systematic categorization of zeolite catalysts is presented below, with the classification being based upon the porosity.

2.3.1. Large-pore zeolites (e.g., *MOR, BEA)*

Large-pore zeolites facilitate enhanced molecular diffusion and active site accessibility. In MOR zeolites, the activity order is Co-MOR > Fe-MOR ≫ Ni-MOR, with Co^{2+} and Fe^{3+} facilitating N–O cleavage through redox cycling [131]. The introduction of In^{3+} increases active channel-bound β-type Co^{2+} sites, while La^{3+} and Mo^{6+} stabilize framework-coordinated γ-type Co^{2+}, thereby inhibiting the formation of inactive Co_3O_4 clusters [132]. Fe-BEA exhibits a predominance of highly dispersed FeO_x species within its straight channels [133]. The Fe(II) sites in BEA zeolite undergo framework-induced distortions that favor N_2O binding and isomerization, promoting efficient oxygen transfer [134]. Furthermore, Co-BEA benefits from enhanced Co exchange and N_2O diffusion, achieving 99.6% N_2O conversion at 450 °C with minimal NO_2 byproduct formation (Fig. 8c) [135].

2.3.2. Medium-pore zeolites (e.g., *MFI, FER)*

Medium-pore zeolites impose moderate spatial constraints, which significantly influence the nature and stability of active sites. In Fe-MFI zeolite (Fe-ZSM-5), low-nuclearity Fe_xO_y clusters demonstrate greater activity compared to mononuclear sites [136]. High performance is frequently linked to binuclear [Fe–O–Fe] sites, which reduce the activation barrier for N–O dissociation [137]. Post-synthetic treatments, such as alkaline leaching, can remove Si, introduce mesoporosity, and increase Fe^{2+} concentration, thereby enhancing N_2O activation and O_2 desorption [138]. Acid treatment improves stability and promotes the formation of active Fe_xO_y species by extracting Al and increasing the Si/Al ratio [139]. Furthermore, the utilization of ammonia steam treatments can lead to a significant increase in the number of accessible Fe sites, thereby enhancing the activity of the catalyst [140]. Fe-FER exhibits remarkable activity due to its unique β-site configuration, which enables cooperative N_2O activation [141]. Furthermore, it demonstrates exceptional hydrothermal stability, maintaining over 90% N_2O conversion after 24 days under simulated nitric acid plant conditions, whereas Fe-MFI and Fe-BEA suffer from accelerated deactivation due to Fe agglomeration and structural collapse [142]. In Co-MFI, there is a coexistence of multiple Co species, including surface Co_3O_4, framework-associated $[Co-O-Co]^{2+}/CoO_x$ clusters, and isolated Co^{2+} at exchange sites [143]. The latter are identified as the primary active sites for N_2O decomposition. Cu-MFI (Cu-ZSM-5) benefits from enhanced Cu^+ accessibility, with ion-exchanged catalysts displaying superior low-temperatures performance [144].

2.3.3. Small-pore zeolites (e.g., *CHA)*

The confined environment of small-pore zeolites favors the stabilization of specific, highly active metal sites. In Fe-CHA(SSZ-13), both monomeric and dinuclear Fe sites contribute to activity. Monomeric Fe^{2+} site confined within six-membered rings (6MR) of the chabazite cages acts as the active site (Fig. 8d) [145,146]. Dinuclear $[HO-Fe-O-Fe-OH]^{2+}$ species are particularly stable and to facilitate O_2 desorption, which is the rate-limiting step [147]. A comparative study of Cu, Fe, and Co-exchanged SSZ-13 shows that N_2O decomposition on Cu- and Fe-SSZ-13 follows a dual-site mechanism on dimeric centers (Fig. 8e) [148]. The higher activity of Fe-SSZ-13 is attributed to a lower activation barrier for N−O cleavage

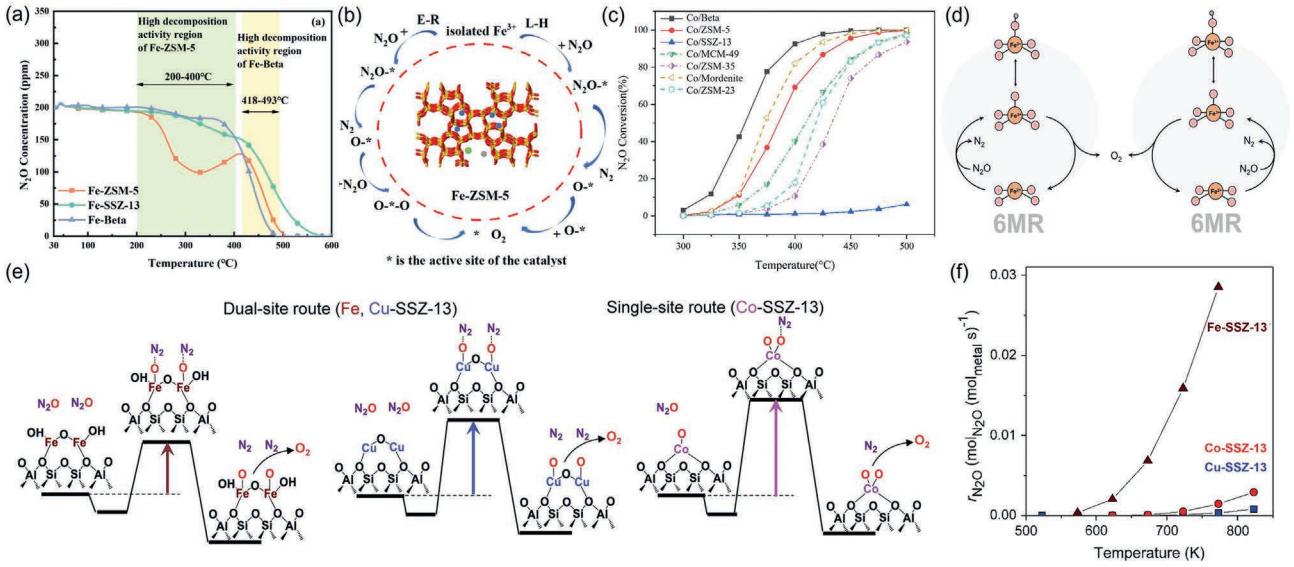


Fig. 8. (a) N_2O conversion of Fe-based zeolites with different topological structures and (b) pathway of N_2O decomposition over Fe-ZSM-5. Reproduced with permission [130]. Copyright 2024, Elsevier. (c) N_2O conversion for Co/zeolites with different topological structures. Reproduced with permission [135]. Copyright 2023, American Chemical Society. (d) Proposed reaction pathway of the N_2O activation and decomposition on the Fe-SSZ-13 catalyst on two adjacent Fe_{6MR} sites. Reproduced with permission [146]. Copyright 2025, American Chemical Society. (e) Reaction site mechanism and (f) rate of N_2O decomposition on Fe-, Co-, Cu-SSZ-13 catalysts. Reproduced with permission [148]. Copyright 2024, Elsevier.

(Fig. 8f). In contrast, Co-SSZ-13 functions *via* a single-site mechanism on isolated Co^{2+}, which results in a higher pre-exponential factor but is counterbalanced by a considerably greater activation energy. Cu-SSZ-13 also demonstrates notable activity, particularly when featuring dimeric [Cu–Cu] sites.

2.4. Emerging catalysts

Recently, the emerging atomic-scale precision engineering and innovative materials and architectures have witnessed the breakthrough in N_2O decomposition. Single-atom catalysts (SACs), such as $Pt_1/MgAl_{1.2}Fe_{0.8}O_4$ and Rh/CeO_2, demonstrate exceptional activity due to optimized metal–support interactions [149,150]. The incorporation of single Pr atoms into Co_3O_4 boosts its activity by 5–7.5 times compared to the pristine oxide (Figs. 9a and b) [151]. Based on the DFT calculations, two-dimensional materials like $Fe@C_2N$ monolayers enable N_2O reduction at ambient temperature, while Co-supported BN systems exhibit distinct configuration-dependent reaction pathways [152,153]. Composite catalysts, including Co_3O_4/g-CN and Ag-modified Co_3O_4/g-CN, show improved low-temperature performance through strengthened Co–N coordination and modulated metal valence states (Fig. 9c) [154,155]. Additionally, high-entropy oxides (HEOs), such as spinel-structured Co-HEOs, have been shown to achieve high N_2O conversion at low temperatures by utilizing multi-element synergy [156]. This enhances reducibility and oxygen vacancy concentration without compromising thermal stability (Figs. 9d-g).

In order to facilitate a more intuitive comparison of N_2O decomposition performance across different catalyst types, Table 1 lists key parameters of representative catalysts reported in recent years [157–164]. Noble metal catalysts exhibit superior low-temperature activity in comparison with other categories, while they suffer from high cost and limited impurity tolerance. Single-metal oxides offer optimal cost-effectiveness, rendering them ideal for medium-temperature and cost-sensitive applications. Co_3O_4 is the most active, and its performance is highly dependent on the synthesis method. However, their performance is often compromised by the presence of O_2 and NO. In the case of composite oxides, the processes of doping and composite formation enhance activity and stability, especially against inhibitors. Hexaaluminates and perovskites exhibit elevated thermal stability, making them well-suitable for high-temperature applications. Zeolite-based catalysts provide well-dispersed active sites. It is evident that the catalytic activity is significantly impacted by the zeolite framework and preparation method. These catalysts frequently exhibit moderately active characteristics, however they can be susceptible to inhibition by O_2 and H_2O. The development of emerging catalysts has enabled the synthesis of catalysts that exhibit both high activity and durability. Especially, Co-HEO demonstrates promising activity and remarkable resistance to a complex gas mixture comprising O_2, NO, and H_2O.

3. Reaction mechanisms

In order to facilitate the rational design of efficient catalysts, the optimization of active sites, and the refinement of reaction pathways for practical applications, it is imperative to comprehensively understand the reaction mechanisms of N_2O decomposition. The direct catalytic decomposition of N_2O typically initiates with its adsorption at an active site (*), resulting in the production of N_2 and an adsorbed oxygen species (O*), as depicted by the following reaction: $N_2O + * \rightarrow N_2 + O^*$. The removal of O* then proceeds *via* two primary pathways: the recombination of two O* species (L–H mechanism) or the reaction between O* and gaseous N_2O (E–R mechanism) (Fig. 10). Finally, O_2 is formed by the recombination of O*, and subsequently desorbs from the surface of the catalyst. This process is widely accepted as the rate-determining step in N_2O decomposition. Indeed, the predominant mechanism is contingent on the catalyst type, the active site structure, and the surface properties.

Mechanistic studies combining theoretical and experimental methods have revealed that charge state and support interactions significantly affect reactivity [165]. For instance, DFT calculations on Rh_6^- and Rh_6^+ clusters have indicated that anionic clusters lower activation barriers for N_2O reduction [166]. *In situ* DRIFTS studies on Ir-supported rutile TiO_2 have demonstrated the formation of peroxide (O_2^{2-}) intermediates, thus highlighting the importance of oxygen spillover and O_v regeneration [39]. An Fe-

Table 1
Performance comparison of different types of N_2O decomposition catalysts.

Catalyst category	Catalysts	Synthesis method	Reaction conditions	Catalytic performance	Publish year	Ref.
Noble metal catalysts	Pd/Al_2O_3	Wet impregnation method	1 % N_2O, He balance, 76,690 h^{-1}	T_{50}: 300 °C; T_{100}: 400 °C	2020	[30]
	Rh/Mg/Al/FeCr alloy foams	Electrodeposition method	1000 ppm N_2O, N_2 balance, 6800 h^{-1}	T_{50}: 320 °C; T_{100}: 400 °C	2020	[31]
	RhO_x/ZrO_2	Impregnation method	1000 ppm N_2O, 10 % O_2, 2 % H_2O, He balance, 100 mL/min	T_{50}: 240 °C; T_{100}: 400 °C	2022	[37]
	Pt-K/SiO_2	Wet impregnation method	2000 ppm N_2O, He balance, 15,000 h_{-1}	T_{50}: 560 °C	2022	[48]
	Ir/LFA, Ir/LMA	Impregnation method	30 vol% N_2O, Ar balance, 100 mL/min, 60,000 cm^{-3} g^{-1} h^{-1}	T_{50}: 284 °C T_{50}: 341 °C	2023	[43]
	$RhO_x/Ag/Al_2O_3$	Impregnation method	0.1 % N_2O, He balance, 100 mL/min	T_{50}: 254 °C; T_{100}: 400 °C	2023	[45]
	Rh/CeO_2	Sol-gel method	1000 ppm N_2O, Ar balance, 30,000 mL g^{-1} h^{-1}	T_{50}: 260 °C; T_{90}: 295 °C	2024	[34]
	Rh(1)–Pd(1)/ZrO_2	Impregnation method	1000 ppm N_2O, He balance, 100 mL/min	T_{50}: 307 °C; T_{90}: 353 °C	2024	[46]
			1000 ppm N_2O, 10 % O_2, 5 % CO_2, 1 % H_2O, He balance, 100 mL/min	T_{50}: 400 °C; T_{90}: 450 °C		
	Rh_{NC}/CeO_2-d	Defects-assisted adsorption method	1000 ppm N_2O, N_2 balance, 120,000 mL g^{-1} h^{-1}	T_{50}: 238 °C	2025	[44]
			1000 ppm N_2O, 5 % O_2, N_2 balance, 120,000 mL g^{-1} h^{-1}	T_{50}: 253 °C		
	Rh(1)/CeO_2-S	Incipient wetness impregnation method and steam-treatment	0.3 % N_2O, He balance, 100 mL/min	T_{50}: 275 °C	2025	[38]
			0.3 % N_2O, 10 % O_2, 5 % CO_2, 1 % H_2O, He balance, 100 mL/min	T_{50}: 425 °C		
	Rh(1)−Ir(1)/ZrO_2	Impregnation method	0.1 % N_2O, He balance, 100 mL/min	T_{50}: 296 °C	2025	[47]
			0.1 % N_2O, 10 % O_2, 5 % CO_2, 1 % H_2O, He balance, 100 mL/min	T_{50}: 385 °C		
Single-metal oxides	Co_3O_4 (nanocube)	Hydrothermal method	30 % N_2O, He balance, 34,000 h^{-1}	T_{50}: 350 °C; T_{100}: 500 °C	2021	[53]
	Co_3O_4 (Yardang Landform structure)	Sol-gel method	2000 ppm N_2O, Ar balance, 20,000 h^{-1}	T_{50}: 300 °C; T_{100}: 400 °C	2023	[54]
	Co_3O_4	PVA-assisted precipitation method	500 ppm N_2O, Ar balance, 400,000 h^{-1}	T_{50}: 425 °C	2024	[57]
	Co_3O_4	Hydrothermal method	1000 ppm N_2O, N_2 balance, 60,000 mL g^{-1} h^{-1}	T_{50}: 350 °C; T_{100}: 450 °C	2024	[59]
	Co_3O_4	Precipitation method and etching	2000 ppm N_2O, N_2 balance, 60,000 mL g^{-1} h^{-1}	T_{50}: 304 °C; T_{90}: 353 °C	2025	[50]
	NiO	Coprecipitation method	1000 ppm N_2O, N_2 balance, 100 mL/min	T_{50}: 366 °C; T_{90}: 419 °C	2023	[98]
	CuO	Citric acid method	2000 ppm N_2O, Ar balance, 20,000 h^{-1}	T_{50}: 455 °C	2023	[90]
Composite oxides	CoCe0.1	Hydrothermal method	2000 ppm N_2O, 2 % O_2, He balance, 38,000 h^{-1}	T_{50}: 365 °C; T_{90}: 420 °C	2020	[78]
	Co_3O_4/m-ZrO_2	Incipient wetness impregnation method	1000 ppm N_2O, Ar balance, 50 mL/min	T_{50}: 375 °C	2020	[94]
	$Co_3O_4/CaCO_3$ ($CaCo_{2.5}$)	Coprecipitation method	2000 ppm N_2O, 2 % O_2, Ar balance, 20,000 h^{-1}	T_{50}: 240 °C; T_{100}: 300 °C	2020	[95]
Composite oxides	$Mg_{0.5}Co$(H-120)	Coprecipitation method	2000 ppm N_2O, Ar balance, 50 mL/min	T_{50}: 240 °C; T_{100}: 300 °C	2021	[157]
	$Ba_{0.5}Co_{2.5}O_4$	Hydrothermal method	0.65 % N_2O, 0.88 % O_2, N_2 balance, 55,000 h^{-1}	T_{90}: 460 °C	2021	[70]
	$Bi_{0.1}NiO_{1.15}$	Coprecipitation method	220 ppm N_2O, N_2 balance, 45,000 h^{-1}	T_{50}: 328 °C; T_{90}: 385 °C	2021	[75]
	$Sm_{0.1}$-Co_3O_4	Sol-gel method	1000 ppm N_2O, N_2 balance, 60,000 mL g^{-1} h^{-1}	T_{50}: 322 °C; T_{90}: 375 °C	2021	[82]
	$Gd_{0.06}Co$	Coprecipitation method	2000 ppm N_2O, Ar balance, 20,000 h^{-1}	T_{50}: 260 °C; T_{90}: 325 °C	2021	[83]
	CeCoAl	Coprecipitation method	1000 ppm N_2O, N_2 balance, 80 mL/min	T_{50}: 300 °C	2021	[87]
	N-Co_3O_4−0.05	g-C_3N_4-modified citrate sol-gel method	1000 ppm N_2O, Ar balance, 10,000 h^{-1}	T_{50}: 320 °C; T_{90}: 360 °C	2021	[102]
	Cs/Co	Coprecipitation method	1000 ppm N_2O, N_2 balance, 30,000 h^{-1}	T_{50}: 225 °C; T_{90}: 250 °C	2022	[66]
	$K_{0.025}Gd_{0.06}Co$	Coprecipitation method	2000 ppm N_2O, Ar balance, 50 mL/min	T_{50}: 225 °C; T_{90}: 275 °C	2022	[158]
			2000 ppm N_2O, 5 vol% O_2, 100 ppm NO, 2 vol% H_2O Ar balance, 50 mL/min	T_{50}: 310 °C; T_{90}: 345 °C		
	Na-Co_3O_4	Hydrothermal method	0.65 vol% N_2O, 0.88 vol% O_2, N_2 balance, 55,000 h^{-1}	T_{50}: 420 °C	2023	[62]
	4Cs/Co_3O_4	Wet impregnation method	1000 ppm N_2O, N_2 balance, 30,000 mL g^{-1} h^{-1}	T_{50}: 272 °C; T_{90}: 349 °C	2023	[67]
	$Ba_{0.2}Cu$	Citric acid method	2000 ppm N_2O, Ar balance, 20,000 h^{-1}	T_{50}: 365 °C; T_{100}: 450 °C	2023	[90]

(*continued on next page*)

Table 1 (*continued*)

Catalyst category	Catalysts	Synthesis method	Reaction conditions	Catalytic performance	Publish year	Ref.
	$Cd_{0.04}Ni$	Coprecipitation method	1000 ppm N_2O, N_2 balance, 30,000 mL g^{-1} h^{-1}	T_{50}: 319 °C; T_{90}: 369 °C	2023	[98]
	$Cs_{0.1}$-Co_3O_4	Citric acid complexation method	200 ppm N_2O, 5 % O_2, N_2 balance, 90,000 h^{-1}	T_{50}: 230 °C; T_{100}: 300 °C	2024	[68]
	Pr_xNi	Coprecipitation method	800 ppm N_2O, N_2 balance, 60,000 mL g^{-1} h^{-1}	T_{100}: 400–440 °C	2024	[84]
	$Bi_{0.015}Co$	Improved sol-gel method	2000 ppm N_2O, Ar balance, 20,000 h^{-1}	T_{100}: 350 °C	2024	[74]
	N-Co_3O_4	g-C_3N_4-modifed thermal decomposition method	1000 ppm N_2O, Ar balance, 10,000 h^{-1}	T_{50}: 270 °C; T_{90}: 350 °C	2024	[159]
			1000 ppm N_2O, 3 vol% O_2, 3.3 vol% H_2O, Ar balance, 10,000 h^{-1}	T_{50}: 365 °C; T_{90}: 450 °C		
	F-Co_3O_4	Coprecipitation method	1000 ppm N_2O, Ar balance, 10,000 h^{-1}	T_{50}: 305 °C; T_{90}: 350 °C	2024	[103]
	Cs-Co_3O_4	Coprecipitation method	200 ppm N_2O, N_2 balance, 90,000 h^{-1}	T_{90}: 297 °C	2025	[69]
			200 ppm N_2O, 5 % O_2, N_2 balance, 90,000 h^{-1}	T_{90}: 281 °C		
	$Cu_{0.15}CoO_y$	Coprecipitation method	500 ppm N_2O, 5 % O_2, Ar balance, 120,000 h^{-1}	T_{100}: 425 °C	2025	[160]
	δ-MnO_2/$Co_{3-x}Mn_xO_4$	Permanganate etching strategy	2000 ppm N_2O, N_2 balance, 60,000 mL g^{-1} h^{-1}	T_{50}: 350 °C; T_{90}: 400 °C	2025	[93]
	$Co_{0.1}$-OMS-2	Sol-gel method	1000 ppm N_2O, Ar balance, 10,000 h^{-1}	T_{90}: 398 °C	2025	[99]
	$K_{0.02}Dy_{0.01}Co$	Coprecipitation method	2000 ppm N_2O, Ar balance, 20,000 h^{-1}	T_{90}: 242 °C	2025	[89]
	$Co_{2.4}Zn_{0.6}O_4$/CeO_2	Citric acid-assisted impregnation method	2000 ppm N_2O, 5 % O_2, Ar balance, 60,000 mL g^{-1} h^{-1}	T_{90}: 442 °C	2025	[101]
	$Eu_{0.04}Ni$	Coprecipitation method	800 ppm N_2O, N_2 balance, 60,000 mL g^{-1} h^{-1}	T_{50}: 325 °C; T_{90}: 357 °C	2025	[85]
			800 ppm N_2O, 5 % O_2, 200 ppm NO, N_2 balance, 60,000 mL g^{-1} h^{-1}	T_{100}: 440 °C		
	Cu(10)/γ-Al_2O_3	Spray coating followed by quick drying	1 % N_2O, N_2 balance, 1800 h^{-1}	T_{50}: 410 °C; T_{90}: 450 °C	2025	[97]
			5000 ppm N_2O, 7.5 % H_2O, air balance, 1800 h^{-1}	T_{50}: 500 °C; T_{90}: 575 °C		
Spinel-structured composite oxides	$ZnCo_2O_4$	Co-precipitation method	500 ppm N_2O, N_2 balance, 15,000 h^{-1}	T_{50}: 178 °C; T_{100}: 250 °C	2024	[110]
	$CuFe_2O_4$	Hydrothermal method with microwave treatment	100 % N_2O, 3000 h^{-1}	T_{50}: 540 °C; T_{100}: 625 °C	2024	[161]
	1K-$Zn_{0.4}Co_{2.6}O_4$	Incipient wetness impregnation method	500 ppm N_2O, N_2 balance, 60,000 h^{-1}	T_{100}: 200 °C	2024	[64]
			500 ppm N_2O, 3 vol% O_2, 6 vol% H_2O, 50 ppm SO_2, N_2 balance, 60,000 h^{-1}	T_{50}: 275 °C; T_{100}: 350 °C		
Perovskite oxides	$LaMnO_3$	Sol-gel method	0.5 % N_2O, 18,000 h^{-1}	T_{50}: 490 °C; T_{90}: 520 °C	2020	[114]
	$PrBaCoO_3$	Supercritical anti-solvent precipitation method	1 % N_2O, He balance, 100 mL/min	T_{50}: 410 °C	2020	[115]
		Citric acid preparation		T_{50}: 445 °C		
	$LaSr_{0.5}CoFe_{0.1}O_{5.8}$	Citric acid preparation	1 % N_2O, He balance, 100 mL/min	T_{50}: 448 °C	2022	[127]
	$LaCo_{0.8}Fe_{0.2}O_3$	Sol-gel method	0.1 vol% N_2O, 5 vol% NO, 6 vol% O_2, 15 vol% H_2O, He balance, 15,000 h^{-1}	T_{50}: 564 °C	2024	[119]
	$LaFe_{0.4}Ni_{0.6}O_3$	Pechini method	0.15 % N_2O, 3 % O_2, 3 % H_2O, He balance, 1000 mL/min	T_{50}: 870 °C	2024	[123]
	$LaCoO_3$/ZrO_2-La	Impregnation method	90 % N_2O, 10 % H_2O, 18,000 h^{-1}	T_{50}: 472 °C; T_{90}: 505 °C	2024	[128]
	$LaCoO_3$	Pechini method	0.15 % N_2O, 3 % O_2, 3 % H_2O, He balance, 1000 mL/min	T_{50}: 785 °C; T_{90}: 890 °C	2025	[122]
	$CaMn_{0.7}Fe_{0.3}O_{3-\delta}$	Pechini method	1000 ppm N_2O, Ar balance, 50,330 h^{-1}	T_{50}: 718 °C	2025	[125]
Zeolite-based catalysts	Fe_1/SAPO-34	Solid-state ion exchange method	500 ppm N_2O, 5 % H_2O, Ar balance, 400,000 h^{-1}	T_{50} > 500 °C; T_{90} > 600 °C	2020	[147]
	Fe_1/SSZ-13					
	FeHZSM-5	Hydrothermal method followed by ion exchange	100 % N_2O, 30,000 mL g^{-1} h^{-1}	T_{100} ≥ 520 °C	2022	[136]
	Co/Beta	Ion exchange method	30 vol% N_2O, He balance, 30,000 h^{-1}	T_{50}: 355 °C; T_{90}: 395 °C	2023	[135]
	Fe-ZSM-5/Fe-SSZ-13/Fe-Beta	Wet impregnation method	200 ppm N_2O, N_2 balance, 30,000 h^{-1}	T_{50}: 330 °C/467 °C/430 °C	2024	[130]
	10Co/HZSM-5	Citric acid-complexion impregnation method	0.65 % N_2O, 0.88 % O_2, Ar balance, 12,000 mL g^{-1} h^{-1}	T_{90}: 430 °C	2024	[143]
	Fe-SSZ-13	One-pot hydrothermal synthesis	500 ppm N_2O, N_2 balance, 100 mL/min	T_{50}: 374 °C	2025	[146]
		Incipient wetness impregnation followed by thermal treatment		T_{50}: 435 °C		
Zeolite-based catalysts	Fe–ZSM-5	Aqueous impregnation method	200 ppm N_2O, 5 % O_2, 100 ppm NO, N_2 balance, 80,000 h^{-1}	T_{50}: 440 °C; T_{100}: 570 °C	2025	[162]
	Fe-MFI/Fe-MOR/Fe-FER/Fe-MRE	Mixed-alkali treatment and wet ion exchange	200 ppm N_2O, Ar balance, 15,000 h^{-1}	T_{50}: 320 °C/387 °C/420 °C/500 °C	2025	[163]
	5 %Fe-FER	Incipient wetness impregnation method	100 % N_2O, 3000 h^{-1}	T_{100}: 460 °C	2025	[164]

(*continued on next page*)

Table 1 (*continued*)

Catalyst category	Catalysts	Synthesis method	Reaction conditions	Catalytic performance	Publish year	Ref.
Emerging catalysts	$Pt_1/MgAl_{1.2}Fe_{0.8}O_4$	Colloid deposition method	1000 ppm N_2O, Ar balance, 20,000 mL g^{-1} h^{-1}	T_{50}: 520 °C; T_{90}: 600 °C	2020	[150]
	Co_3O_4/g-CN	Impregnation method	0.1 vol% N_2O, Ar balance, 10,000 h^{-1}	T_{100}: 400 °C	2021	[154]
	Rh/CeO_2	Incipient wetness impregnation method	0.02 % N_2O, 5 % CO_2, Ar balance, 100,000 mL g^{-1} h^{-1}	T_{50}: 365 °C; T_{90}: 450 °C	2023	[149]
	AgCo-g-CN	Impregnation method	500 ppm N_2O, 3 % O_2, N_2 balance, 30,000 h^{-1}	T_{100}: 400 °C	2024	[155]
	Co-HEO	Coprecipitation method	1000 ppm N_2O, 5 % O_2, 800 ppm NO, 4.2 % H_2O, N_2 balance, 100 mL/min	T_{50}: 313 °C; T_{90}: 356 °C	2024	[156]

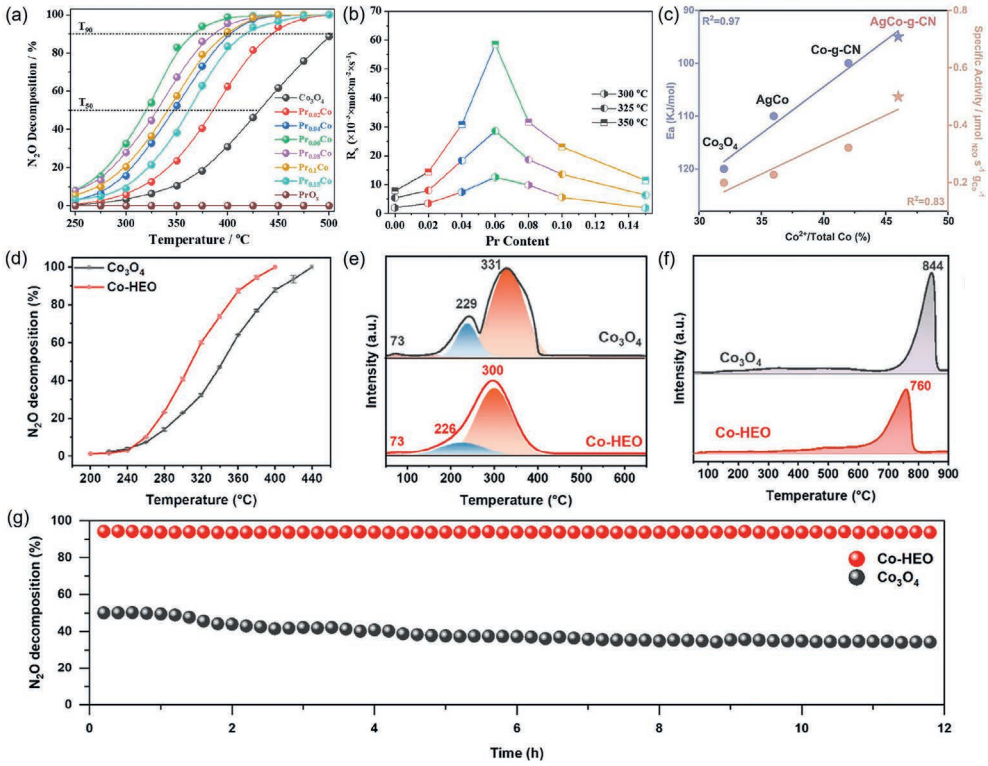


Fig. 9. (a) N_2O decomposition activity and (b) reaction rates normalized by S_{BET} on Co_3O_4 and Pr-doped Co_3O_4 samples. Reproduced with permission [151]. Copyright 2022, American Chemical Society. (c) Relationship between the content of Co^{2+} and the specific activity or the energy of activation for N_2O decomposition. Reproduced with permission [155]. Copyright 2024, Elsevier. (d) Catalytic activity of Co_3O_4 and Co-HEO for N_2O decomposition, (e) H_2-TPR, (f) O_2-TPD of Co_3O_4 and Co-HEO, and (g) Stability test of Co_3O_4 and Co-HEO at 360 °C. Reproduced with permission [156]. Copyright 2024, American Chemical Society.

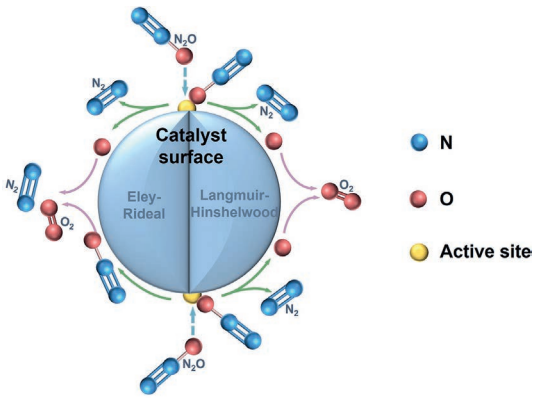


Fig. 10. Representative reaction mechanisms of N_2O decomposition.

substituted La-hexaaluminate-supported Ir catalyst (Ir/LFA) operates *via* a dual-path mechanism: N_2O dissociation on Ir and O_v-mediated oxygen transfer has been shown to achieve high activity ($T_{50} = 284$ °C) [43]. On defect-rich CeO_2-supported Rh SACs, the L–H mechanism dominates, with O_v facilitating oxygen transfer and recombination (Fig. 11a) [44]. Redox mechanisms involving O_v govern N_2O decomposition on metal oxides. In the Cu_xCo_y mixed oxides, Co_3O_4 supplies O_v for N_2O adsorption, forming □-Co-ON_2 species, while the interfacial CuO_x promotes N–O cleavage (Fig. 11b) [91]. Kinetic and DFT analyses reveal first-order kinetics with N_2O concentration, identifying N–O cleavage as the rate-determining step. Similarly, in the Cu/CeO_2 system, binuclear $[Cu–O–Cu]^{2+}$ sites on CeO_2 {100}/{110} planes have been shown to drive the reaction, facilitated by the presence of Ce^{3+}/Ce^{4+} redox cycling (Fig. 11c) [167]. Nevertheless, the presence of H_2 has been demonstrated to cause dissociative adsorption on O_v, resulting in the competition between NO and active oxygen, which consequently leads to the reversible deactivation of the catalyst. In the context of Co-doped CeO_2, an increase in O_v density has been demonstrated to lower the light-off temperature ($T_{90} = 375$ °C) and improve stability [168]. Notably, the doping of Zn introduces a dual modulation mechanism for the Co_3O_4/CeO_2 catalyst: it alters the geometric/electronic structure of Co sites and enhances

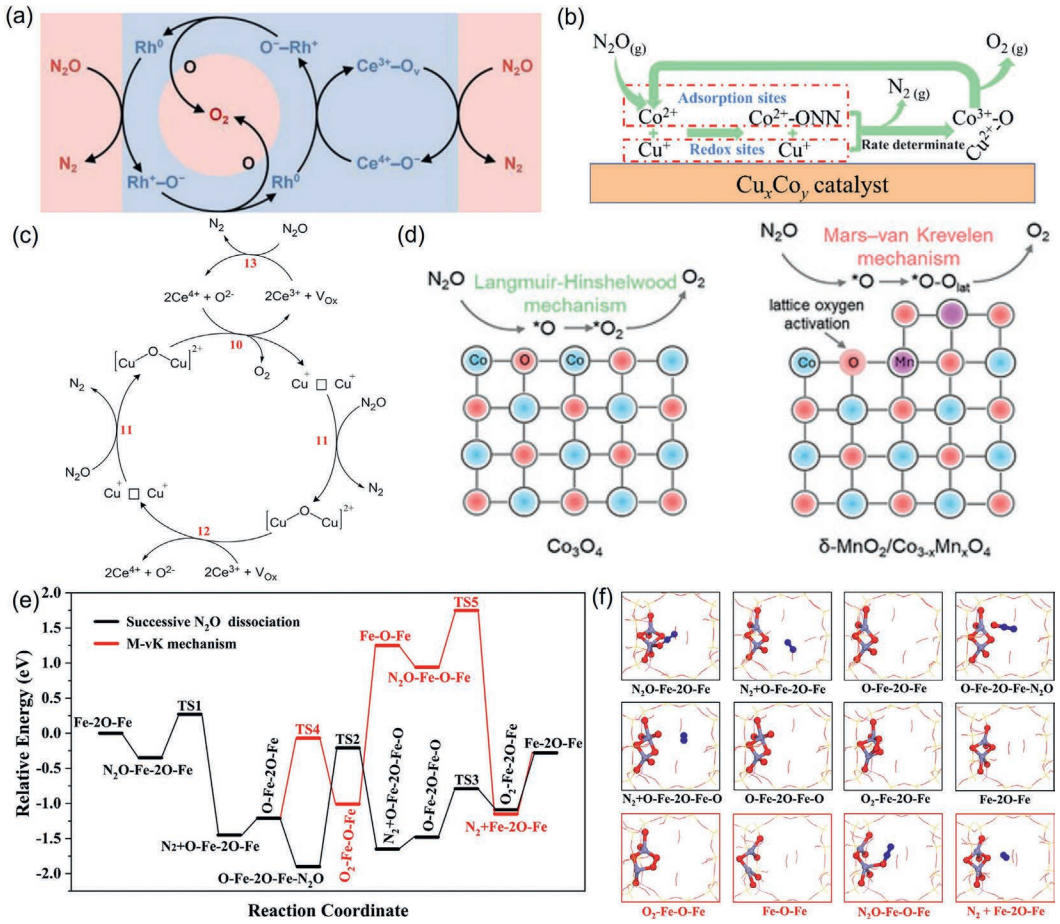


Fig. 11. (a) Main mechanism of catalytic N_2O decomposition on Rh_{NC}/CeO_2-d. Reproduced with permission [44]. Copyright 2025, Elsevier. (b) Key roles of CuO and Co_3O_4 in the Cu_xCo_y catalysts for N_2O decomposition. Reproduced with permission [91]. Copyright 2019, American Chemical Society. (c) Proposed mechanism of N_2O decomposition over CuO/CeO_2 catalyst. Reproduced with permission [167]. Copyright 2016, Elsevier. (d) Different reaction mechanism for δ-$MnO_2/Co_{3-x}Mn_xO_4$ and pristine Co_3O_4. Reproduced with permission [93]. Copyright 2025, John Wiley & Sons. (e) Calculated energy profile and (f) intermediate structures for N_2O decomposition on Fe–2O–Fe/SSZ-13. Red, gray-purple, and blue balls represent O, Fe, and N atoms, respectively. Reproduced with permission [147]. Copyright 2020, Elsevier.

electron injection from CeO_2, collectively leading to an electron-rich Co_3O_4 and increased O_v. This synergy effectively overcomes the energy barrier limiting the N–O activation and cleavage rate-determining step [101]. In Mn-modified Co_3O_4, the heterointerface between δ-MnO_2 and $Co_{3-x}Mn_xO_4$ enhances Co 3d–O 2p hybridization and Co–O–Mn covalency, generating highly active lattice oxygen near the interface [93]. Isotope studies have confirmed a shift from the L–H mechanism on pristine Co_3O_4 to a dominant lattice-oxygen-mediated Mars-van Krevelen pathway, leading to improved N_2O decomposition activity and stability (Fig. 11d). The presence of "boxed dot-Co^{2+}" sites in Cu-doped Co_3O_4 has been identified through *in situ* DRIFTS, which has detected trans-$N_2O_2^-$ as an intermediate [160]. Perovskites, such as $LaMnO_{3+\delta}$, have been demonstrated to have high oxygen mobility, as evidenced by isotopic exchange ($^{18}O_2/N_2{}^{16}O$), thereby enabling efficient lattice oxygen involvement [169].

Transition metal-exchanged zeolites, such as those containing Fe, Cu, and Co, have been observed to exhibit metal-specific mechanisms that are sensitive to nuclearity and zeolite topology. In Rh- and Fe-modified ZSM-5, transient product analysis distinguishes between pathways: Rh-ZSM-5 follows the E–R mechanism, while Fe-ZSM-5 adheres to the L–H mechanism [170]. Mononuclear Fe sites have been found to present high activation barriers (>180 kJ/mol), whereas binuclear clusters promote O_2 release through spin-crossover cycles [171]. In Fe/CHA catalysts (*e.g.*, SAPO-34, SSZ-13), dinuclear $[HO–Fe–O–Fe–OH]^{2+}$ species enhance both O_2 desorption and stability (Figs. 11e and f) [147]. Cu-ZSM-5 zeolites operate *via* dimeric $[Cu–Cu]^{2+}$ sites using an E–R mechanism [172,173]. For Co-zeolites, isolated Co^{2+} ions are active, but their aggregation into Co_3O_4 results in diminished performance [148].

Notably, the reaction mechanisms of emerging N_2O decomposition catalysts vary across different systems. In Rh/CeO_2 SACs, the promotion of O_v formation and enhancement of redox properties is observed to be a consequence of engineered Rh–O coordination [149]. The doping of single Pr atoms into Co_3O_4 results in the formation of a "Pr 4f-O 2p-Co 3d" electronic network, which redistributes electron density redistribution to Co^{2+} sites, thereby reducing the N–O cleavage barrier [84]. In the case of Co-supported BN systems, the catalysts exhibit configuration-dependent pathways: CoN_3 sites follow an E–R mechanism, whereas CoB_3 sites adopt L–H kinetics [153]. Spinel-structured Co-HEOs achieve high conversion rates at low temperatures and maintain thermal stability at high temperature due to the enhanced reducibility and O_v concentration through multi-element synergy [156].

The mechanistic insights discussed above provide a fundamental blueprint for the rational design of next-generation N_2O decomposition catalysts. A central tenet is that O_2 desorption is often the rate-determining step, which directly informs strategies such as weakening metal–O bonds *via* alkali metal promoters (Section 2.2.2-(1)) or facilitating O_2 release through O_v generation using redox-active dopants (Section 2.2.2-(2)). Moreover, the highly active of binuclear sites in zeolites emphasizes the critical need

Table 2
Key mechanistic steps and regulation mechanisms for different N_2O decomposition catalysts.

Catalyst category	Active site combination	N_2O activation mode	O^* desorption regulation mechanism	Rate-determining step
Noble metal catalysts	Metal sites+support O_v	Metal-support electronic interaction weakens N−O bonds	Support O_v accepts O^* to lower desorption energy	O^* desorption from support O_v
Transition metal oxide catalysts	Metal ions+O_v	Metal ions donate electrons; O_v adsorbs N_2O	Redox cycles regenerate O_v	O^* desorption from O_v
Zeolite-based catalysts	Mono-/binuclear metal sites	Binuclear sites synergistically reduce activation energy of N−O dissociation	Zeolite pore confinement promotes O^* recombination	O^* desorption
Emerging catalysts	Metal ions+O_v	Coordination environment and electronic structure reduce activation energy	Metal ions modulate O_v electron density	O^* desorption

to control the nuclearity and coordination environment of metal cations during synthesis (Section 2.3). As outlined in Table 2, the predominant pathway, whether L−H or E−R, and the pivotal mechanistic steps are found to be contingent on the catalyst's architecture. Noble metal catalysts depend on efficient N_2O dissociation at metal sites in conjunction with oxygen spillover to O_v-rich supports. Conversely, transition metal oxide catalysts are governed by redox cycles that hinge on the formation and replenishment of O_v. Zeolite-based catalysts exhibit metal-specific mechanisms that are sensitive to the nuclearity of active sites (mono- *vs.* binuclear) and the confinement effect of the zeolite topology. The advent of novel materials, such as SACs, underscores the significance of meticulously customizing the coordination environment and electronic structure to optimize reaction pathways. In conclusion, a targeted manipulation of the catalyst structure, guided by a deep mechanistic understanding, is the key to overcoming the activity and stability bottlenecks in N_2O decomposition.

4. The practice of direct decomposition catalysts

Based on the extensive theoretical research, various catalysts have been investigated for practical engineering applications [174]. Indeed, the performance of N_2O decomposition catalysts under real industrial conditions and in engineering applications is influenced by multiple factors, including catalyst composition, support material, operating temperature, and the presence of inhibitors. The Pd/Al_2O_3 catalyst exhibited high activity in the monopropellant thruster, sustaining N_2O decomposition at efficiencies >75 % and temperatures >1500 K [175]. This high performance, which is attributed to a reduction in activation energy under elevated pressure, positions it as a viable substitute for toxic hydrazine propellants. Catalysts, such as $K/Zn-Co_3O_4$ and K-doped Co−Mn−Al mixed oxides derived from hydrotalcite precursors, have been validated in pilot-scale nitric acid plants [176,177]. These materials maintain N_2O conversions above 70 %–90 % at 400–450 °C under realistic tail gas conditions containing O_2, H_2O, NO_x, and NH_3, with operational stability exceeding 10 weeks. In the context of high-temperature applications (750−900 °C), such as in the production of nitric acid *via* ammonia oxidation, FeO_x/Al_2O_3 catalysts supported on metastable Al_2O_3 (δ, θ-Al_2O_3) exhibit remarkable stability and activity, sustaining over 90 % N_2O conversion for more than 12 days under realistic gas mixtures containing NO, O_2, and H_2O [178].

5. Challenges and perspectives

The development of efficient N_2O decomposition catalysts faces several critical challenges, including limited activity and stability, incomplete mechanistic understanding, and insufficient scalability. For instance, catalyst deactivation often occurs under practical conditions due to competitive adsorption of H_2O and O_2 inhibition at O_v sites. To address these issues, innovative materials designs, such as the core-shell structures, are being explored to protect active sites from poisoning. As highlighted in above discussions, the rate-determining step in N_2O decomposition is typically O_2 desorption. Catalytic performance is thus strongly influenced by the oxygen adsorption and desorption properties of the active sites. Only when these properties are optimally tuned can high catalytic activity be achieved. Accordingly, for novel catalysts (particularly the multicomponent catalyst systems, such composite oxides, spinel-structured composite oxides, perovskite oxides, and high-entropy oxides), rational design strategies should prioritize the modulation of oxygen interaction energetics through advanced computational approaches. Machine learning-guided catalyst discovery has demonstrated considerable promise in accelerating the identification of optimal compositions and structures with improved activity and durability. In parallel, fundamental gaps remain in elucidating the dynamic behavior of active sites under working conditions. The deployment of advanced *in situ*/*operando* characterization techniques, such as DRIFTS, XAS, and environmental TEM, is essential to monitor structural evolution in real time and identify key reactive intermediates throughout the catalytic cycle. These insights are critical for the rational design of next-generation catalysts that combine high activity and stability with reduced economic and environmental impacts.

Nowadays, emerging strategies for N_2O elimination, such as solar-thermal activation and plasma-assisted decomposition, leverage renewable energy sources to enable more sustainable and energy-efficient emission control, in alignment with global energy transition trends to reduce the carbon footprint of industrial processes. Scaling up these technologies requires careful balancing of the catalytic performance with scaling feasibility. A thorough techno-economic analysis (TEA) is essential to evaluate synthesis costs, catalyst lifetime, regeneration needs, and energy consumption under realistic operating conditions. Notably, a significant trade-off exists between noble-metal-based catalysts (which often exhibit superior activity at higher costs) and transition-metal-based alternatives. The latter may offer improved economic sustainability, though often at the expense of lower tolerance to feed variability or reduced stability. Concurrently, a full life cycle assessment (LCA) is needed to quantify environmental impacts across all stages, from raw material extraction and catalyst production to deactivation and disposal or recycling. Such a comprehensive evaluation ensures that the net environmental benefit of N_2O abatement is not offset by hidden burdens associated with energy-intensive synthesis or the use of scarce resources.

CRediT authorship contribution statement

Yingxue Lu: Writing – original draft, Visualization, Formal analysis, Data curation, Conceptualization. **Ying Xin:** Writing – review & editing, Validation, Supervision, Resources, Funding acquisition, Conceptualization. **Hao Wu:** Visualization, Formal analysis,

Data curation. **Jin Wang:** Methodology, Formal analysis. **Zhaoliang Zhang:** Writing – review & editing, Supervision, Funding acquisition.

Declaration of competing interest

The authors declare that they have no known competing financial interests or personal relationships that could have appeared to influence the work reported in this paper.

Acknowledgments

This work was funded by National Natural Science Foundation of China (Nos. 22376078 and 22276070), Taishan Scholar Program of Shandong Province (Nos. tsqn202408207 and tstp20230628), Shandong Provincial Natural Science Foundation (Nos. ZR2023ZD39 and ZR2024MB064).

References

[1] United Nations Environment Programme and Food and Agriculture Organization of the United Nations, 2024, Global Nitrous oxide assessment, https://doi.org/10.59117/20.500.11822/46562.
[2] H. Tian, R. Xu, J.G. Canadell, et al., Nature 586 (2020) 248–256.
[3] M.J. Prather, J. Hsu, N.M. DeLuca, et al., J. Geophys. Res.: Atmos. 120 (2015) 5693–5705.
[4] X. Cui, S. Chen, J. Yang, et al., J. Environ. Manag. 377 (2025) 124580.
[5] S. Christensen, K. Rousk, iScience 27 (2024) 109042.
[6] G. Zhu, H. Shi, L. Zhong, et al., Nat. Rev. Earth Environ. 6 (2025) 574–592.
[7] R. Feng, Z. Li, Environ. Pollut. 338 (2023) 122664.
[8] Regulation (EU) 2024/1257 of the European Parliament and of the Council, Official Journal of the European Union, 2024. http://data.europa.eu/eli/reg/2024/1257/oj.
[9] Action Plan for Nitrous Oxide Emission Control in the Industrial Sector, Ministry of Ecology and Environment of China, National Development and Reform Commission of China, and Ministry of Industry and Information Technology of China, 2025. https://www.mee.gov.cn/xxgk2018/xxgk/xxgk03/202508/t20250829_1126396.html.
[10] Z. Zhuang, B. Guan, J. Chen, et al., Chem. Eng. J. 486 (2024) 150374.
[11] J. Quan, R. Yin, Z. Zhao, et al., J. Am. Chem. Soc. 145 (2023) 12044–12050.
[12] M.L. Ovcharov, V.M. Granchak, Theor. Exp. Chem. 57 (2021) 30–63.
[13] X. Zhang, Y. Wang, Y. Wang, et al., Chem. Commun. 58 (2022) 2777–2787.
[14] M. Liu, H. Zhang, J. Li, et al., ChemCatChem 16 (2024) e202400922.
[15] A. Shigemoto, Y. Sekine, Chem. Commun. 61 (2025) 1559–1573.
[16] X. Wu, J. Du, Y. Gao, et al., Chem. Soc. Rev. 53 (2024) 8379–8423.
[17] Y. Zhang, J. Du, Y. Shan, et al., Chem. Soc. Rev. 54 (2025) 1151–1215.
[18] M. Qian, B. Guan, Z. Zhuang, et al., Catal. Sci. Technol. 15 (2025) 2061–2103.
[19] L. Wang, C. Lin, I. Boldog, et al., Angew. Chem. Int. Ed. 63 (2024) e202317435.
[20] K.H. Kang, M. Yang, S. Raza, et al., Chemosphere 335 (2023) 139114.
[21] Z. Li, Y. Wu, H. Wang, et al., Environ. Sci. Technol. 58 (2024) 8976–8987.
[22] L.S. Ko, Y.S. Chen, K.L. Pan, et al., Catal. Commun. 177 (2023) 106666.
[23] A. Shigemoto, T. Higo, C. Ukai, et al., Catal. Sci. Technol. 14 (2024) 4471–4478.
[24] Z. Liu, F. He, L. Ma, et al., Catal. Surv. Asia 20 (2016) 121–132.
[25] R. Zhang, N. Liu, Z. Lei, et al., Chem. Rev. 116 (2016) 3658–3721.
[26] Y. Zhang, Z. Tian, L. Huang, et al., Catalysts 13 (2023) 943.
[27] H. Yu, X. Wang, X. Wu, et al., Chem. Eng. J. 334 (2018) 800–806.
[28] M. Jabłońska, R. Palkovits, Catal. Sci. Technol. 6 (2016) 7671–7687.
[29] V.G. Komvokis, M. Marti, A. Delimitis, et al., Appl. Catal. B: Environ. 103 (2011) 62–71.
[30] N. Richards, J.H. Carter, E. Nowicka, et al., Appl. Catal. B: Environ. 264 (2020) 118501.
[31] P.H. Ho, M. Jabłońska, R. Palkovits, et al., Chem. Eng. J. 379 (2020) 122259.
[32] S.S. Kim, S.J. Lee, S.C. Hong, J. Ind. Eng. Chem. 18 (2012) 1263–1266.
[33] C. Sui, F. Yuan, Z. Zhang, et al., Catalysts 6 (2016) 173.
[34] H. Liu, S. Yang, J. Mi, et al., Environ. Sci. Technol. 58 (2024) 17125–17136.
[35] M. Piumetti, M. Hussain, D. Fino, et al., Appl. Catal. B: Environ. 165 (2015) 158–168.
[36] H. Liu, Y. Lin, Z. Ma, Chin. J. Catal. 37 (2016) 73–82.
[37] Y. Jing, K. Taketoshi, N. Zhang, et al., ACS Catal. 12 (2022) 6325–6333.
[38] N. Zhang, C. He, Y. Jing, et al., Angew. Chem. Int. Ed. 64 (2025) e202517403.
[39] E. Pachatouridou, E. Papista, A. Delimitis, et al., Appl. Catal. B: Environ. 187 (2016) 259–268.
[40] I.V. Yentekakis, G. Goula, P. Panagiotopoulou, et al., Appl. Catal. B: Environ. 192 (2016) 357–364.
[41] H. Liu, Z. Ma, Chin. J. Chem. Eng. 26 (2018) 109–115.
[42] C. Sui, X. Niu, Z. Wang, et al., Catal. Sci. Technol. 6 (2016) 8505–8515.
[43] M. Wang, W. Li, S. Wang, J. Phys. Chem. C 127 (2023) 20344–20353.
[44] S. Bao, X. Lu, L. Yu, et al., Appl. Catal. A: Gen. 693 (2025) 120122.
[45] Y. Jing, C. He, N. Zhang, et al., ACS Catal. 13 (2023) 12983–12993.
[46] N. Zhang, C. He, Y. Jing, et al., Surf. Interfaces 46 (2024) 104120.
[47] N. Zhang, C. He, Y. Jing, et al., Environ. Sci. Technol. 59 (2025) 1598–1607.
[48] B. Bozorgi, J. Karimi-Sabet, P. Khadiv-Parsi, Environ. Technol. Innovation 26 (2022) 102344.
[49] M. Konsolakis, ACS Catal. 5 (2015) 6397–6421.
[50] Y. Long, X. Zhu, C. Gao, et al., Nat. Commun. 16 (2025) 1048.
[51] Z. Ma, Y. Ren, Y. Lu, et al., J. Nanosci. Nanotechnol. 13 (2013) 5093–5103.
[52] P. Stelmachowski, K. Ciura, G. Grzybek, Catal. Sci. Technol. 6 (2016) 5554–5560.
[53] M. Li, R. Zhang, H. Wang, et al., Catal. Today 376 (2021) 177–187.
[54] H. Yu, X. Qi, X. Du, et al., Mol. Catal. 537 (2023) 112960.
[55] Ž. Chromčáková, L. Obalová, F. Kovanda, et al., Catal. Today 257 (2015) 18–25.
[56] H. Li, L. Zheng, T. Zhao, et al., J. Fuel Chem. Technol. 46 (2018) 717–724.
[57] S. Li, J. Zhao, Z. Song, et al., Fuel 362 (2024) 130745.
[58] Y. Wang, X. Wei, X. Hu, et al., Catal. Lett. 149 (2019) 1026–1036.
[59] H. Ou, Y. Yue, T. Yang, et al., ACS ES T Eng. 5 (2024) 1032–1042.
[60] P. Stelmachowski, G. Maniak, A. Kotarba, et al., Catal. Commun. 10 (2009) 1062–1065.
[61] L. Nowakowski, C. Hudy, F. Zasada, et al., J. Am. Chem. Soc. 146 (2024) 24450–24466.
[62] J. Sun, A. Song, Y. Tian, et al., ChemCatChem 15 (2023) e202201449.
[63] G. Maniak, P. Stelmachowski, F. Zasada, et al., Catal. Today 176 (2011) 369–372.
[64] H. Prajitno, J. Kim, M.H. Jeong, et al., Chemosphere 367 (2024) 143642.
[65] G. Grzybek, J. Gryboś, P. Indyka, et al., Appl. Catal. B: Environ. 297 (2021) 120435.
[66] F. Zhao, D. Wang, X. Li, et al., Ind. Eng. Chem. Res. 61 (2022) 13854–13862.
[67] Y. Gong, Z. Liu, Z. Li, et al., Environ. Sci. Technol. 58 (2023) 906–914.
[68] H. Zhao, P. Wang, Z. Li, et al., J. Environ. Chem. Eng. 12 (2024) 113907.
[69] H. Zhao, P. Wang, Z. Li, et al., Aerosp. Sci. Technol. 166 (2025) 110522.
[70] J. Sun, L. Wang, L. Zhang, et al., ACS Appl. Energy Mater. 4 (2021) 8496–8505.
[71] Q. Zhang, X. Tang, P. Ning, et al., RSC Adv. 5 (2015) 51263–51270.
[72] H. Yu, X. Wang, X. Wu, Mol. Catal. 460 (2018) 69–73.
[73] L. Xue, H. He, C. Liu, et al., Environ. Sci. Technol. 43 (2009) 890–895.
[74] K. Wang, Y. Du, Y. Li, et al., Mol. Catal. 569 (2024) 114604.
[75] M. Xu, H. Wang, H. Ouyang, et al., J. Hazard. Mater. 401 (2021) 123334.
[76] Y. Wang, X. Hu, K. Zheng, et al., Catal. Commun. 111 (2018) 70–74.
[77] M.G. Jung, J.E. Seo, H.P. Ha, et al., Chem. Eng. J. 505 (2025) 159305.
[78] C. He, A. Li, Z. Liu, Catal. Surv. Asia 24 (2020) 232–238.
[79] M. Lykaki, E. Papista, N. Kaklidis, et al., Catalysts 9 (2019) 233.
[80] M. Zabilskiy, P. Djinović, E. Tchernychova, et al., ACS Catal. 5 (2015) 5357–5365.
[81] Z. Liu, C. He, B. Chen, et al., Catal. Today 297 (2017) 78–83.
[82] H. Liu, J. Chen, Y. Wang, et al., Chem. Eng. J. 414 (2021) 128643.
[83] Y. Xiong, Y. Zhao, X. Qi, et al., Environ. Sci. Technol. (2021) 13335–13344.
[84] Z. Zhang, Y. Wu, Y. Sun, et al., ACS ES T Eng. 4 (2024) 2542–2552.
[85] S. Cao, Z. Zhang, Y. Wu, et al., J. Colloid Interface Sci. 696 (2025) 137880.
[86] P.H. Ho, M. Jabłońska, M. Nocuń, et al., ChemCatChem 11 (2019) 5580–5592.
[87] P.H. Ho, M. Jabłońska, G. Beltrami, et al., J. Mater. Sci. 56 (2021) 15012–15028.
[88] F. Zhang, X. Wang, X. Zhang, et al., Chem. Eng. J. 256 (2014) 365–371.
[89] H. Yu, Y. Li, Y. Pan, et al., Chem. Eng. J. 504 (2025) 159032.
[90] Y. Li, X. Wang, C. Shi, J. Environ. Chem. Eng. 11 (2023) 109970.
[91] S. Xiong, J. Chen, N. Huang, et al., Environ. Sci. Technol. 53 (2019) 10379–10386.
[92] Y. Wang, X.L. Liu, X. Hu, et al., React. Kinet. Mech. Catal. 129 (2019) 165–179.
[93] Y. Long, Y. Peng, Y. Bai, et al., Angew. Chem. Int. Ed. 64 (2025) e202516326.
[94] X. Hu, Y. Wang, R. Wu, et al., Appl. Surf. Sci. 514 (2020) 145892.
[95] H. Yu, X. Wang, Y. Li, Catal. Today 339 (2020) 274–280.
[96] P. Zhao, F. Qin, Z. Huang, et al., Catal. Sci. Technol. 8 (2018) 276–288.
[97] E.H. Lee, I.H. Kwak, H. Kim, et al., J. Mater. Chem. A 13 (2025) 5056–5067.
[98] F.L. Zhao, C. Wang, D. Wang, et al., Appl. Catal. A: Gen. 649 (2023) 118946.
[99] H. Dang, L. Li, H. Sun, et al., J. Colloid Interf. Sci. 680 (2025) 699–711.
[100] C. Zhang, Z. Zhang, C. Sui, et al., ChemCatChem 8 (2016) 2155–2164.
[101] H. Liu, S. Cheng, J. Chen, et al., Environ. Sci. Technol. 59 (2025) 22927–22939.
[102] X. Hu, Y. Wang, R. Wu, et al., Mol. Catal. 509 (2021) 111656.
[103] R. Wu, Q. Wang, R. Wang, et al., ChemCatChem 17 (2024) e202401659.
[104] J.J. Torrez-Herrera, S.A. Korili, A. Gil, Catal. Rev. 64 (2020) 592–630.
[105] M. Santiago, J. Pérez-Ramírez, Environ. Sci. Technol. 41 (2007) 1704–1709.
[106] Y. Zhang, X. Wang, Y. Zhu, et al., J. Phys. Chem. C 118 (2014) 1999–2010.
[107] Y. Zhu, X. Wang, G. Wu, et al., J. Phys. Chem. C 116 (2011) 671–680.
[108] R. Li, Y. Li, Z. Liu, Fuel 355 (2024) 129405.
[109] B.M. Abu-Zied, S.A. Soliman, S.E. Abdellah, Chin. J. Catal. 35 (2014) 1105–1112.
[110] H. Prajitno, J. Kim, M.H. Jeong, et al., Fuel 371 (2024) 132053.
[111] R. Amrousse, T. Katsumi, Catal. Commun. 26 (2012) 194–198.
[112] M. Jabłońska, R. Palkovits, Catal. Sci. Technol. 9 (2019) 2057–2077.
[113] J. Simböck, M. Ghiasi, S. Schönebaum, et al., Nat. Commun. 11 (2020) 652.
[114] R.H. Blackmore, M.E. Rivas, G.F. Tierney, et al., Phys. Chem. Chem. Phys. 22 (2020) 18774–18787.
[115] N. Richards, J.H. Carter, L.A. Parker, et al., ACS Catal. 10 (2020) 5430–5442.
[116] P. Bělina, G. Sádovská, V. Krejčíková, et al., J. Therm. Anal. Calorim. 138 (2019) 4197–4202.
[117] X. Gao, Y. Li, J. Chen, et al., Mol. Catal. 510 (2021) 111713.
[118] A.G. Margellou, T.C. Vaimakis, P.J. Pomonis, et al., React. Kinet., Mech. Catal. 127 (2019) 825–838.
[119] P. Zheng, F. He, Y. Wu, et al., ChemistrySelect 9 (2024) e202304026.
[120] S. Kumar, A. Vinu, J. Subrt, et al., Catal. Today 198 (2012) 125–132.
[121] K.L. Pan, S.J. Yu, S.Y. Yan, et al., J. Air Waste Manage. 64 (2014) 1260–1269.
[122] L.A. Isupova, Y.A. Ivanova, I.P. Prosvirin, et al., Kinet. Catal. 66 (2025) 297–311.

[123] L.A. Isupova, Y.A. Ivanova, I.P. Prosvirin, et al., Dalton Trans. 53 (2024) 15273–15283.
[124] C. Huang, Y. Zhu, X. Wang, et al., J. Catal. 347 (2017) 9–20.
[125] A. Serrano-Lotina, E. Mastronardo, J.M. Coronado, Appl. Catal. A: Gen. 689 (2025) 120026.
[126] H. Arandiyan, S.S. Mofarah, C.C. Sorrell, et al., Chem. Soc. Rev. 50 (2021) 10116–10211.
[127] N. Richards, L.A. Parker, J.H. Carter, et al., Catal. Lett. 152 (2021) 213–226.
[128] P. Zemlianskii, D. Morozov, G. Kapustin, et al., Colloid. Surf. A 698 (2024) 134546.
[129] D.V. Ivanov, L.G. Pinaeva, L.A. Isupova, et al., Appl. Catal. A: Gen. 457 (2013) 42–51.
[130] A. Li, P. Wang, L. Zhang, et al., Fuel 378 (2024) 132888.
[131] D. Pietrogiacomi, M.C. Campa, L.R. Carbone, et al., Appl. Catal. B: Environ. 240 (2019) 19–29.
[132] X. Zhang, Q. Shen, C. He, et al., Chem. Eng. J. 226 (2013) 95–104.
[133] B. Chen, N. Liu, X. Liu, et al., Catal. Today 175 (2011) 245–255.
[134] M.L. Bols, B.E.R. Snyder, H.M. Rhoda, et al., Nat. Catal. 4 (2021) 332–340.
[135] B. Kang, R. Zhang, M. Guo, et al., Energ. Fuel 37 (2023) 18019–18029.
[136] A.A. Gainanova, G.M. Kuz'micheva, L.V. Pirutko, et al., J. Mater. Res. 38 (2022) 532–546.
[137] G. He, B. Zhang, H. He, et al., Sci. Total Environ. 673 (2019) 266–271.
[138] B. Louis, F. Ocampo, H.S. Yun, et al., Chem. Eng. J. 161 (2010) 397–402.
[139] M. Wu, H. Wang, L. Zhong, et al., Chin. J. Catal. 37 (2016) 898–907.
[140] X. Liang, H. Tang, F. Yang, et al., Micropor. Mesopor. Mat. 290 (2019) 109655.
[141] K. Jíša, J. Nováková, M. Schwarze, et al., J. Catal. 262 (2009) 27–34.
[142] E. Tabor, G. Sádovská, M. Bernauer, et al., Appl. Catal. B: Environ. 240 (2019) 358–366.
[143] S. Li, J. Wang, R. Su, et al., Mol. Catal. 552 (2024) 113706.
[144] S.A. Yashnik, A.V. Salnikov, N.T. Vasenin, et al., Catal. Today 197 (2012) 214–227.
[145] J.B. Lim, S.H. Cha, S.B. Hong, Appl. Catal. B: Environ. 243 (2019) 750–759.
[146] D.C. Cano-Blanco, J.W.A. Fischer, F. Buttignol, et al., ACS Catal. 15 (2025) 15579–15595.
[147] T. Zhang, Y. Qiu, G. Liu, et al., J. Catal. 392 (2020) 322–335.
[148] F. Lin, T. Andana, Y. Wu, et al., J. Catal. 401 (2021) 70–80.
[149] S. Xie, D. Kim, K. Ye, et al., J. Rare Earth. 41 (2023) 941–951.
[150] K. Liu, Y. Tang, Z. Yu, et al., Sci. China Mater. 63 (2020) 949–958.
[151] H. Liu, S. Yang, G. Wang, et al., Environ. Sci. Technol. 56 (2022) 16325–16335.
[152] X. Liu, L. Sheng, Mater. Today Commun. 28 (2021) 102585.
[153] W. Qu, C. Wang, P. Wang, et al., Appl. Surf. Sci. 636 (2023) 157792.
[154] X. Hu, Y. Wang, R. Wu, et al., Appl. Surf. Sci. 538 (2021) 148157.
[155] Y. Yin, R. Xiao, L. Qiu, et al., Fuel 366 (2024) 131303.
[156] B. Li, X. Duan, T. Zhao, et al., Environ. Sci. Technol. 58 (2024) 2153–2161.
[157] Y. Li, F. Tang, D. Wang, et al., Catal. Sci. Technol. 11 (2021) 3737–3745.
[158] Y. Xiong, Y. Zhao, W. Shan, et al., Chemosphere 303 (2022) 135257.
[159] X. Hu, J. Meng, L. Feng, et al., Catal. Lett. 154 (2024) 4367–4377.
[160] Y. Zhang, Q. Dong, J. Zhang, et al., Catal. Sci. Technol. 15 (2025) 3848–3858.
[161] P. Zemlianskii, D. Morozov, G. Kapustin, et al., Ceram. Int. 50 (2024) 34081–34090.
[162] A. Li, P. Wang, T. Yan, et al., Aerosp. Sci. Technol. 164 (2025) 110394.
[163] H. Yang, D. Cheng, Q. Zhang, et al., J. Environ. Chem. Eng. 13 (2025) 117715.
[164] A. Makova, O. Tkachenko, G. Kapustin, et al., Arab. J. Sci. Eng. 51 (2026) 1391–1400.
[165] L.Y. Wu, C. Chen, L. Luo, et al., ChemistrySelect 5 (2020) 5391–5399.
[166] H. Francisco, V. Bertin, J.R. Soto, et al., J. Phys. Chem. C 120 (2016) 23648–23659.
[167] M. Zabilskiy, P. Djinović, E. Tchernychova, et al., Appl. Catal. B: Environ. 197 (2016) 146–158.
[168] X. Wang, R. Duan, Z. Li, et al., Environ. Sci. Technol. 59 (2025) 5839–5847.
[169] D.V. Ivanov, L.G. Pinaeva, E.M. Sadovskaya, et al., J. Mol. Catal. A: Chem. 412 (2016) 34–38.
[170] E. Kondratenko, V. Kondratenko, M. Santiago, et al., J. Catal. 256 (2008) 248–258.
[171] G. Li, E.A. Pidko, I.A.W. Filot, et al., J. Catal. 308 (2013) 386–397.
[172] K.M. Farhan, P.K. Sajith, Ind. Eng. Chem. Res. 64 (2025) 5257–5268.
[173] M.L. Tsai, R.G. Hadt, P. Vanelderen, et al., J. Am. Chem. Soc. 136 (2014) 3522–3529.
[174] F. Buttignol, P. Biasi, A. Garbujo, ACS ES T Eng. 5 (2025) 2170–2180.
[175] G.D. Di Martino, G. Gallo, S. Mungiguerra, et al., Acta Astronaut. 180 (2021) 460–469.
[176] M. Inger, M. Wilk, M. Saramok, et al., Ind. Eng. Chem. Res. 53 (2014) 10335–10342.
[177] K. Pacultová, K. Karásková, F. Kovanda, et al., Ind. Eng. Chem. Res. 55 (2016) 7076–7084.
[178] G. Sádovská, E. Tabor, M. Bernauer, et al., Catal. Sci. Technol. 8 (2018) 2841–2852.